Post-Processing of Data Gathered Using Tomographic Particle Image Velocimetry on a Phantom of an Intracranial Aneurysm.

Hemo-dynamic Quantaties: Wall Shear Stress, Time Averaged WSS, Oscillating shear index and the Transverse WSS.

Diederik Portheine – 4492676

Bachelor Thesis

Applied Physics

Delft, 29-06-2020

Assoc. Prof. Dr. S. Kenjereš

Acknowledgements

This bachelor thesis was carried out, in strong collaboration with Stijn de Haan. Due to the Covid-19 situation it was not possible to attend The Transport Phenomena (TP) Group of the TU Delft but still I felt a part of it due to the weekly zoom meetings which were hosted every Thursday.

The research was supervised by S. Kenjereš. I would like to start to express my appreciation to Saša for giving me the opportunity to write my Bachelor Thesis in his group. Because of his self-directing approach I was able to make a lot of decisions concerning the research and was therefore free in concentrating on the possibilities. I found our meetings very pleasant, informative and very motivating in conducting and developing the research. I will definitely recommend Saša to my fellow students.

Next, I want to express my gratitude towards Xiaolin Wu. Her help and great knowledge on the subject of aneurysms has made this research a great and informative experience. Also, many thanks for helping us out with Tecplot and for all your enormous amount of PIV-related knowledge. I hope our research can help your PHD and that some day your PHD will do lots of good on the insights on the rupture risk of intracranial aneurysms and how to prevent rupture to save lives.

Abstract

The third biggest cause of death in the western world is the stroke which is often caused by an aneurysm. Recent literature proposes the Wall Shear Stress (WSS), the Time-Averaged Wall Shear Stress (TAWSS), the Oscillatory Shear Index (OSI) and the Transverse WSS (Trans-WSS) as possible factors influencing the initiation, growth and rupture of intracranial aneurysms (IA). Currently, scientist and doctors are still in disagree on the biggest factors of rupture of an IA.

In this research project, Tomographic Particle Image Velocimetry (TPIV) is used to acquire data to calculate these before mentioned hemodynamic quantities. The experiment captured 2040 images during one simulated cardiac cycle in a phantom reflecting an IA. To obtain the WSS, TAWSS, OSI and Trans-WSS on the wall of the phantom these images were post-processed using Davis, Tecplot and Python. The hemodynamic quantities are successfully calculated and visualized on 3D models of the aneurysm.

An accurate result for these hemodynamic quantities was achieved when using a minimum of 51 images evenly spread out during a cardiac cycle. In cases without time constraints, it is still recommended to use as many images as possible to account for local WSS fluctuations. In further research the data structure in DaVis should be altered to a constant Cartesian coordinate structure for every dataset of the phantom. This will remove the biggest error and will greatly increase the value of this thesis and the analysis of these quantities.

Summary

The third biggest cause of death in the western world has changed over the last decades. Cancer, stroke and heart attacks are now the biggest contributor. Researching these causes is currently top priority. Yet still there is much unknown. The stroke, regularly caused by an intracranial aneurysm is one of these causes that is under lots of investigation. Scientist and doctors around the world are researching the risk analysis of unruptered aneurysms to help prevent rupture in the future. In the investigation on these aneurysms multiple experimental research methods exist. One of these methods is Tomographic Particle Image Velocimetry which is used to help investigate this origin of the stroke and help analyse the blood flow in an aneurysm using high speed cameras to follow tracer particles which are added to the fluid. In this thesis, The data gathered using Tomographic Particle Image Velocimetry is post processed to further analyse the blood flow inside the aneurysm. In this research it is tried to calculate such called hemo-dynamic quantities which may help the risk analysis of rupture which regularly lead to death. The data for this research is gathered using a scaled model of a real aneurysm in which it is tried to simulate the pulsating blood flow using so called fluid mechanics dimensionless key figures. The acquired data is post processed to further analyse the rupture risk inside an aneurysm. Currently, scientist and doctors are still in disagree on the biggest factors of rupture of an intracranial aneurysm. It is believed that the Wall Shear Stress plays a major role. Further on in this thesis the following hemo-dynamic quantities will be calculated: Wall Shear Stress, Time Averaged Wall Shear Stress, Oscillating Shear Index and the Transverse Wall Shear Stress. The results of these hemo-dynamic quantities are displayed on 3D models of the aneurysm. In addition, it was researched how many data is needed to post process and to correctly analyze these hemo dynamics quantities. It is found that for a simulated cardiac cycle of 2040 pictures (T=5.1 sec) more then 50 evenly spaced points in between is enough to give an accurate visualization of these hemo-dynamic quantities. However, when computational power and storage space is not an issue it is recommended to add more data points in between to have better insight into the local fluctuations inside the aneurysm. All these post processing steps are done using multiple programs and coding. One of these languages was Python which was used to alter the data when Tecplot was limited to do so. The language and coding was not the hardest part of this research but the data management was. My recommendation to further analyse these hemo-dynamic quantities is to alter the data in a earlier stage such that the structure of the data is rigid and constant for every time point. This will remove the biggest error and will greatly increase the value of the results and the analysis of these hemo-dynamic quantities.

Contents

1 Introduction

1.1 General Introduction

The cause of most long-term neurological deficits and the third biggest origin of death in the Western World is the stroke. One kind of stroke is the subarachnoid hemorrhage (SAH), which often is an aftereffect of the rupture of an intracranial aneurysm which causes 500.000 deaths worldwide every year [1]. About one third of the survivors of these ruptures suffer from permanent disabilities [2]. Autopsy studies have revealed that intracranial aneurysms occur in 2 - 3 % of the general population. luckily, 50-80 % of all existing aneurysms do not rupture during a persons lifetime [3][4].

An Aneurysm is a weakened spot of the artery wall which results into a bulge of the artery. Most of the aneurysms can be found in the circle of Willis, which is an important part of the artery network in the brain [4]. How to manage unruptured aneurysms is still highly debated in the medical world. Most common used treatments for unruptured aneurysms are further monitoring, surgical clipping or endovascular procedures like coiling or implanting flow diverters. To this date, the choice of treatment is mainly based on the size and location of the aneurysms even though research has shown that hemodynamic quantities, such as the wall shear stress, play a crucial role in the rupture of an aneurysm [2][5].

Nowadays, more and more literature proposes that hemodynamics play a major role in the development, growth and rupture of intracranial aneurysms and the underlying biological processes of arterial wall degradation. These literature rely on experiments conducted on (model) aneurysms or analytical computational methods [6] [7].

Some of the hemodynamic parameters which influence the aneurysm are the Wall Shear Stress (WSS), the Oscillating Shear Index (OSI), the time-averaged wall shear stress (TAWSS) and the Transverse WSS (Trans-WSS) [8][9]. All these criteria can be obtained using tomographic Particle Image Velocimetry (TPIV), which is a non-invasive and optical flow measurement technique [10].

Particle Image Velocimetry (PIV) refers to a class of methods allowing for the calculation of instantaneous velocity vector fields, through a measurement of the displacement of fine particles that are seeded into the fluid. The tracer particles are illuminated twice within a short time interval. When doing this the location is captured and the displacement of the particles can be determined. Eventually, this can be used to calculate their local velocity, and hence the local flow velocity of the fluid [11].

With the gathering of further data and more research on these criteria, better simulations can be made which are able to effectively predict a patient-specific flow profile and the corresponding hemodynamic quantities inside an aneurysm. With this knowledge, a proper risk assessment and a decision regarding the optimal treatment can be made which could save lives. This research has been conducted from 20th of April until the 29th of June in collaboration with Stijn de Haan.

1.2 Motivation

In previous studies into this topic, the subject of the causes for a rupture in an intracranial aneurysm are still unclear and often contradictory. One of these causes is said to be hidden in the flow characteristics of an aneurysm. With researching the intracranial aneurysm and computing physical quantities we can shed light on the cause of rupture of an intracranial aneurysm which is a very lethal event that can happen to a human being. When more becomes known about the flow characteristics inside an aneurysm then as a result will the risk assessment improve. Consequently will the choice in treatment improve which could save a lot of lives.

1.3 Research Goal

Before this research, 2040 pictures of a phantom reflecting an intracranial aneurysm are taken during one cardiac cycle using tomographic PIV. These pictures are then processed in computer software to get the velocity fields. In this research, it will be explored to what extent the following hemodynamic parameters: the Wall Shear Stress, the Time-Averaged Wall Shear Stress, the Oscillatory Shear Index and the Transverse Wall Shear Stress can be retrieved from these velocity fields that were calculated. Secondly, the amount of velocity fields or timepoints needed to achieve a proper result of these hemodynamic parameters, that contains all information of the cardiac cycle, will be studied. This is important as post-processing all 2040 velocity fields is not possible because this requires too much computational power and memory.

1.4 Thesis Outline

This thesis is structured by firstly discussing the fundamentals of an intracranial aneurysm and the hemodynamic theory. Thereafter, the used Tomographic Particle Image Velocimetry system will be described and explained. Furthermore, the experimental method will be outlined, where the manner in which the experiment has been conducted will be presented and how it is post processed. This is followed by the results, their discussion and the possible improvements and future recommendations. These will be used to make conclusions regarding our aforementioned research goal.

2 Theoretical Background

In the following sections, the theoretical background is described of the fields this research touches upon. This includes information on intracranial aneurysms and their rupture risk, hemodynamics (blood-dynamics) and particle image velocimetry.

2.1 Biomedical Background of Intracranial Aneurysms.

An aneurysm is a local bulge or thinned out-pouching in a blood vessel wall and its size can range from a couple of millimeters to a few centimeters. When an aneurysm is located in the brain it is called an intracranial aneurysm and these intracranial aneurysms are often situated in the Circle of Willis or in the arteries that are connected to the Circle of Willis [2][4]. The Circle of Willis plays an important role in the research on intracranial aneurysm and is therefore explained in more detail in the next subsection.

2.1.1 Circle of Willis

The Circle of Willis is a cerebral arterial circle [12]. In figure 1, a schematic overview of the Circle of Willis is shown. In this figure, it is clear that the Circle of Willis has a circular shape as its name suggests. Blood from the heart arrives at the Circle of Willis through the Basilar Artery on the posterior side and through the left and right Internal Carotid Arteries on the anterior side. The blood leaves the Circle of Willis through six major arteries which branch into smaller arteries that supply the oxygen for 80 % of the brain. The circular shape of the Circle of Willis functions as a compensatory mechanism for supplying the entire brain with oxygen in the case of occlusion or stenosis in one of the supplying arteries. The Circle of Willis also protects the cerebral artery from hemodynamic stress and pressure differences as blood arrives in the skull through different arteries asynchronously. [13][14].

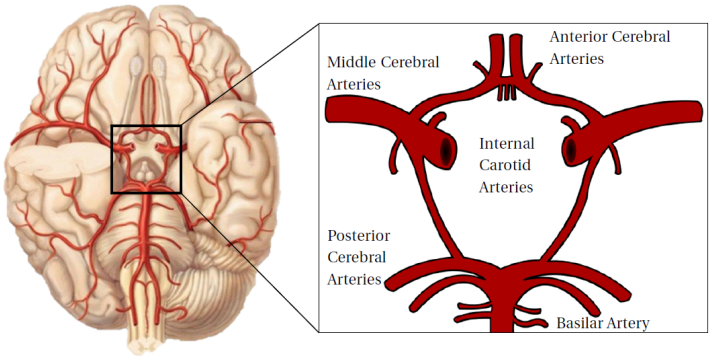

Figure 1: The location of the Circle of Willis inside the brain. On the right a schematic overview of all arteries at the Circle of Willis is given [15].

In approximately 70 % of individuals an incomplete Circle of Willis is observed where some of the arterial components are absent or developed incompletely. As a result, neighboring arteries take over functions of other arteries and grow in size. This phenomenon requires the ability of the arterial walls to adapt to those circumstances [12][16].

Arterial walls consist of three layers: the tunica adventitia, the tunica media and the tunica intima. The tunica adventitia is the outermost layer and is composed of fibro-elastic connective fiber which connects the artery to surrounding tissue. The tunica media is the middle and thickest layer of the arterial wall and contains predominantly smooth muscle cells embedded in elastic fiber. This layer is responsible for the change in diameter of the artery to change the flow rate. The tunica intima is the innermost layer which is in direct contact with the blood. This layer consists of a single layer of endothelial cells and a thin fibro-elastic tissue layer [14][17].

2.1.2 Origin and growth of intracranial aneurysms

An aneurysm can be saccular or fusiform. Both types can be seen in figure 2. Saccular aneurysms only bulge out on one side of the artery whereas a fusiform aneurysm balloons out in all directions. The saccular intracranial aneurysm is the most common type of intracranial aneurysm and it is also the focus of this research [3].

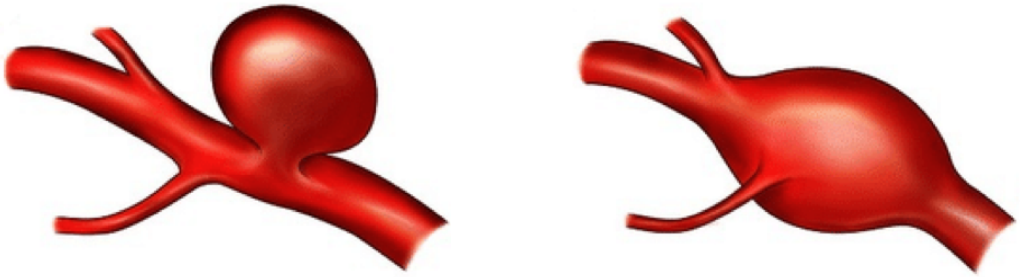

(a) Saccular Aneurysm (b) Fusiform Aneurysm

Figure 2: Two types of aneurysms. Source: https://openi.nlm.nih.gov

The origin and growth of an intracranial aneurysm has been studied less than the cause of rupture [5]. The exact cause of intracranial aneurysms is unknown, but a general consensus is found in the cause being a result of the combination of hemodynamics, arterial wall composition, genetics and cell populations [6]. Intracranial aneurysms are commonly seen at bifurcations and sharp curves of arteries at the Circle of Willis. At these impingement points there is a complex hemodynamic environment and this observation implies that hemodynamics play a major role in initiation and growth of intracranial aneurysms [7][14]. The risk of having an intracranial aneurysm is also influenced by other factors such as gender, age, smoking and family members with intracranial aneurysms [4][3].

In aneurysm walls, it is observed that the tunica media, which contains all muscle cells, is decreased in size which causes structural defects [2][7]. As a result, the tunica adventitia, which is the stiff layer outside of the artery, becomes the most important load bearing layer in the walls of intracranial aneurysms [6].

2.1.3 Rupture Risk

As 2-3 % of the general population carries intracranial aneurysms, it is crucial to identify driving forces of rupture and this is the reason the governing factors of rupture risk are studied extensively [3][5]. An intracranial aneurysm will either grow until a state of homeostatic stability is reached or until the wall strength can no longer withstand the hemodynamic stress. Where in the last case rupture occurs [6][7].

The factors for rupture of an intracranial aneurysm are discussed controversially. Multiple factors linked to aneurysmal rupture are proposed. These are the resulting wall composition, aneurysm size and shape, the presence of a daughter sac, the location of the aneurysm and again hemodynamic factors [3][5][6][18]. Meng et al. [7] proposed a triangular relationship between aneurysm geometry, flow in an aneurysm and the pathobiology of the aneurysmal wall. In this triangular relationship, flow exerts forces on the vessel wall. Now as flow changes this will result in remodeling of the wall. As a result of wall remodeling the geometry of the aneurysm will change which in turn changes the flow again. This is a positive feedback loop which could eventually cause rupture in an intracranial aneurysm. The hemodynamic factors influencing initiation, growth and rupture of intracranial aneurysms will be discussed in the next section.

2.2 Hemodynamics

The fluid dynamics that is dealt with when modelling blood flow is called hemodynamics. In fluid dynamics, an important material property is viscosity. When a fluid has a constant viscosity at all rates of shear, it is called a Newtonian fluid. Blood is composed of blood plasma and several kinds of formed elements in this plasma. The formed elements consist of erythrocytes or red blood cells, white blood cells and platelets which all have an influence on the flow behavior of blood. As a result, blood can often be seen as a non-Newtonian fluid. This distinction can be done accordingly to shear rates. Shear rate is the rate at which a fluid is sheared or "worked" during flow. In more technical terms, it is the rate at which fluid layers or laminae move past each other. Shear rate is determined by both the geometry and speed of the flow. However for the case of our aneurysm, at shear rates higher than 100 s^{-1} can the viscosity of blood be regarded as constant in large and medium sized arteries. Below a shear rate of 100 s^{-1} will the red blood cells form aggregates and this increases the viscosity [19]. According to Razavi et al. [20] when the shear rates in the Circle of Willis are higher than 100 s^{-1} then this means that the blood can be approximated as a Newtonian fluid with a constant viscosity of 0.0035 Pa $\cdot$ s. However, the shear rate during a cardiac cycle is not always greater than 100 s^{-1} so this approximation is not always accurate [19]. In the next subsections will the fundamental equations for fluid flow, dynamic similarity and fluid parameters for rupture be discussed.

2.2.1 Fundamental Equations

The flow of blood can, like other fluid flows, mathematically be described with the conservation of energy, conservation of mass, conservation of momentum and other information and formulas for the specific situation. The most important ones are the equations for the conservation of mass and the conservation of momentum. The conservation of mass is expressed by the continuity equation/

$$\frac{\partial \rho}{\partial t} + \nabla \cdot (\rho \vec{v}) = 0 \tag{1}$$

where ρ is the density of the fluid and $\vec{v}$ is the velocity of the fluid. The conservation of momentum is represented by the Navier-Stokes equations:

$$\rho(\frac{\partial \vec{v}}{\partial t} + \vec{v} \cdot \nabla \vec{v}) = -\nabla p + \mu \nabla^2 \vec{v} + \rho \vec{g} \tag{2}$$

where p is pressure, μ is the viscosity of the fluid and $\vec{g}$ is the acceleration vector due to gravity. The results of the Navier-Stokes equations give a vector field of the flow velocity [21].

2.2.2 Dynamic Similarity

In this research, a phantom of a cerebral artery with an aneurysm is constructed. To achieve the same flow in the phantom as for in an actual artery, geometric and dynamic similarity is needed. The geometry of the phantom is the same as an actual artery the only difference is that the dimensions of the phantom are larger which as a consequence alters the flow. For dynamic similarity, the flow characteristics through the phantom have to be the same as for the actual artery. This is done by keeping the value of the Reynolds number and Womersley number the same for the dynamics inside phantom as for the dynamics inside the actual artery [22][23].

The Reynolds number is an important dimensionless number which can be seen as the ratio between inertial forces and viscous forces of a flow. The Reynolds number is defined as

$$Re = \frac{\rho v D}{\mu} \tag{3}$$

where ρ is the density of the fluid, v is the velocity, D is the characteristic length and μ is the viscosity of the fluid. For the flow of blood in an artery the characteristic length is the diameter of this artery. In the formula for the Reynolds number it is evident that the Reynolds number does not only depend on the fluid but also depends on the systems dimensions. The Reynolds number categorizes a flow as laminar, turbulent or in the transition range between laminar and turbulent flow. For each system with different dimensions two different turning points for the Reynolds number can be found. When the Reynolds number is below the lower critical Reynolds number $Re_{crit,lower}$ of a system, a flow is laminar and the fluid moves sheet-like as the viscous forces are large compared to the inertial forces. In contrary, when the Reynolds number is higher than the upper critical Reynolds number $Re_{crit,upper}$ of a certain system the flow is turbulent. In a turbulent flow the viscous forces are too small to keep the flow controlled and now the flow moves in swirls [21]. In figure 3 the differences between a laminar and a turbulent flow are shown. From an MRI scan of a patient was found that the Reynolds number in a cerebral artery is approximately between 180 and 350 which means the blood flow is laminar[24].

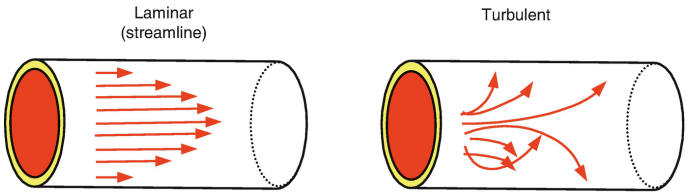

Figure 3: A laminar and turbulent flow schematically shown [25].

The Womersley number is the dimensionless number that is used to characterize the pulsating flow in the artery and its definition is stated in the following equation.

$$\alpha = \frac{D}{2}\sqrt{\frac{\rho\omega}{\mu}} \tag{4}$$

where D, ρ and μ are the same as in Reynolds number and where ω is the angular frequency of the pulsating flow. The Womersley number characterizes a pulsatile flow by the ratio of transient inertial forces and viscous forces that account for the angular frequency of the flow. The Reynolds number is dependent on the velocity of the blood so it varies during the cardiac cycle. The Womersley number, on the other hand, remains constant during the cardiac cycle and only changes with the diameter of the artery [23].

2.2.3 Wall Shear Stress

The arterial walls experience two kinds of forces. The first one is the normal stress on the wall as a result of blood pressure. The second force is the tangential stress along the wall which is called the Wall Shear Stress (WSS) and depends on the viscosity of the blood [19]. WSS is the most controversial and highlighted hemodynamic parameter associated with aneurysm growth and rupture [7].

The WSS is stated in the equation below.

$$WSS = \tau_w = \mu \cdot \dot{\gamma}_w = \mu\frac{dv_w}{dz_w} \tag{5}$$

where μ is the viscosity of the fluid, $\dot{\gamma}_w = \frac{dv_w}{dz_w}$ is the wall shear rate or velocity gradient near the wall, v_w is velocity parallel to the wall and z_w is the perpendicular distance to the wall. As blood in this research is considered as a Newtonian fluid the WSS is linear to the wall shear rate $\dot{\gamma}_w$. However, approximating blood to be a Newtonian fluid may cause WSS measurements to be inaccurate in regions of low shear [8].

WSS works directly on the cells of the endothelium in the tunica intima of an artery. A certain level of WSS in an artery (which differs for every artery) is beneficial for maintaining the structure. However, when the WSS differs from this level it can trigger the endothelial cells to pathological responses. When the WSS is at a high value, the endothelial cells discharge nitrogen oxide which causes the vessel wall to dilate. As a result, the diameter of the artery increases and the WSS decreases [26]. This is a remarkable conclusion that blood vessels are capable to alter their dimensions to change the values of WSS on their wall.

WSS plays an important role in origin of aneurysms. Multiple studies show that very high levels of WSS and WSS gradients were found at sites of future aneurysms. High levels of WSS lead to media thinning and bulge formation which are the earliest signs of an aneurysm [27][28][29]. The role of WSS in growth and rupture of aneurysms is inconsistent and vague. Studies reported that

both high and low WSS influenced aneurysm growth and rupture. Some studies concluded that low WSS facilitates growth, triggers rupture and causes degenerative modifications in endothelial cells [30][31]. On the other hand, different studies found that aneurysm rupture is correlated with high WSS [32][33][34]. Meng et al. [7] proposed that both high and low WSS can tip the balance of vascular homeostasis and drive aneurysm growth and rupture.

2.2.4 Time-Averaged WSS, Oscillatory Shear Index and the Transverse WSS

Due to the pulsating nature of blood flow, other parameters were proposed to evaluate the WSS on the arterial wall such as the Time-Averaged Wall Shear Stress (TAWSS), Oscillatory Shear Index (OSI) and the Transverse Wall Shear Stress (Trans-WSS).

The TAWSS is the time-averaged magnitude of the WSS over the cardiac cycle and is defined as below.

$$TAWSS = \frac{1}{T}\int_0^T |\vec{\tau}_w|\, dt \tag{6}$$

where T is the total time of the cardiac cycle [8]. The OSI measures the directional change of WSS during a cardiac cycle. This index van be seen as the disturbance of the direction of the flow [31]. The OSI is defined as below.

$$OSI = \frac{1}{2}\left[1 - \left(\frac{\left|\int_0^T \vec{\tau}_w dt\right|}{\int_0^T |\vec{\tau}_w|\, dt}\right)\right] \tag{7}$$

If the OSI is large ($OSI \approx 0.5$) it is said to be a flow with almost maximum directional change and thus no mean shear direction. If the OSI is small ($OSI \approx 0$) then the flow is uni-directional and thus does therefore have zero directional change on average [8][35].

Several studies concluded that a high OSI together with a low TAWSS are highly correlated to aneurysmal rupture [6][31][36]. Xiang et al. [31] identifies OSI and TAWSS as the most significant variables for rupture of aneurysms in the hemodynamic field. However, the OSI does not distinguish well between uniaxial pulsatile flow and multidirectional flow. To quantify this directional of the disturbed flow a new hemodynamic quantity is introduced, the Transverse Wall Shear Stress (Trans-WSS). The Trans-WSS is the average over the cardiac cycle of WSS components perpendicular to the temporal mean WSS vector, with which endothelial cells are assumed to align [37]. This quantity was recently reintroduced by Veronique Peiffer [38].

$$transWSS = \frac{1}{T}\int_0^T \left|\vec{\tau}_\omega \cdot (\vec{n} \times \frac{\int_0^T \vec{\tau}_\omega dt}{\left|\int_0^T \vec{\tau}_\omega dt\right|})\right| dt \tag{8}$$

$$transWSS = \frac{1}{T}\int_0^T \left|\vec{\tau}_\omega \cdot (\vec{n} \times \frac{\vec{\tau}_{mean}}{|\vec{\tau}_{mean}|})\right| dt \tag{9}$$

Here $\vec{n}$ represents the normal vector to the surface of the aneurysm.

The Trans-WSS can take any value from 0 to the TAWSS. When the Trans-WSS is low this indicates that the flow, which can be steady, pulsatile or oscillatory, remains approximately parallel along to a single axis throughout the cardiac cycle [38]. Whereas a High trans-WSS is accounted to: large fluctuations of a small shear vector, small fluctuations of a large shear vector, or small fluctuations of a moderate shear vector over a large part of the cardiac cycle. Furthermore, Trans-WSS does not completely characterize the dynamics of the WSS. It cannot distinguish between an unidirectional flow and reversing but uniaxial flow. Both of these situations result in a Trans-WSS of zero as can be seen in figure 4 [39]. However, Trans-WSS does distinguish between uniaxial and multidirectional flows even when they have the same OSI. Therefore it does not replace the TAWSS, OSI, but rather complements them [9][40].

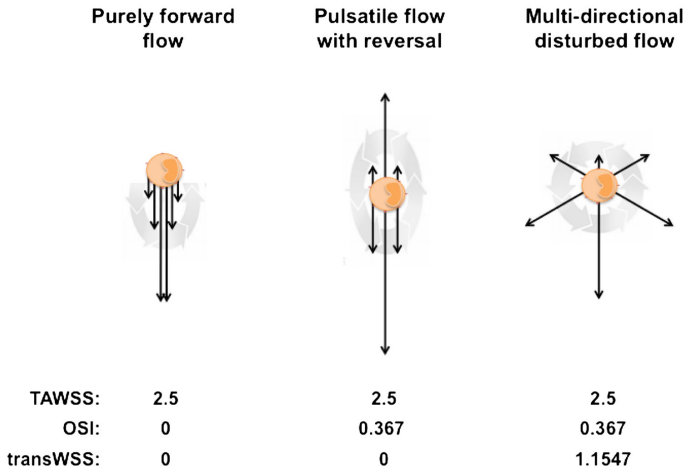

Figure 4: Three different flow environments to which an endothelial cell could be exposed. The black arrows represent WSS vectors at various times in the cardiac cycle. The grey arrows indicate their evolution with time. The table lists TAWSS (Pa), OSI and Trans-WSS (Pa) for the three environments. Values in table are from [38].

2.2.5 Discrete time integration

For the calculation of the previously stated hemodynamic quantities integration is needed. However, in this research and in most experimental fluid mechanical research this is not possible due to the fact that the data is given in a discrete domain. To still be able to calculate an integration the assumption of Quadrature rules based on interpolations was used (midpoint/rectangle rule) [41]. This assumption is shown in the following equation.

$$\int_a^b f(x)dx \approx \frac{(b-a)}{N} \sum_{n=1}^{N} f_i[x] \tag{10}$$

With N the amount of evenly spaced points on the domain [a b].

2.3 Measurement methods

In experimental fluid mechanics different types of measurement methods are used to study the flow in systems and determine the instantaneous field of velocity vectors. These methods can be separated into two different categories, intrusive and non-intrusive methods. The key difference between these categories is that for the intrusive methods the flow is altered and therefore the system is not an accurate model and events that happen in the system are less accurate in contrary to non-intrusive methods. Commonly, the methods that are used in the biomedical sector are seen as non-intrusive [42][43][44]. As for measurements on intracranial aneurysms three methods are widely used: Stereo Particle Image Velocimetry (SPIV), Tomographic Particle Image Velocimetry (TPIV) and a non-experimental method one called Computational Fluid Dynamics (CFD) [11].

The particle image velocimetry class uses high speed cameras to take consecutive images of (tracer) particles to follow and capture the flow. These particles are small enough not to disturb the flow and it therefore mostly falls in the Stokes-regime. As a result, the disturbance due to the particles in the flow is so small that this is negligible and the method can be seen as a non-intrusive method. Using this method the position and speed of the particle is measured. With Stereo-PIV two cameras are used to view the system in an illuminated plane from two different angles. The in-plane velocity is separately computed from each camera and then is used for reconstructing the velocity vectors in every dimension. However, with Tomographic-PIV three velocity vectors are all retrieved from the system due to smart optimisation of cameras and their angles [45][46]. For highly three-dimensional flows this can lead to substantial measurement errors of the local velocity vector [47]. TPIV uses a combination of camera' and mirrors to measure the position and velocity in all three dimensions. This method is more accurate then SPIV but adds more computational complexity to the processing process. CFD is the analytic method of calculating the flow properties for every location at every time. This is often the most accurate method and has more possibilities then PIV. However, it does require more computing power then the other methods [48]. In figure 5 below are the pros and cons of the different measurement types visualized.

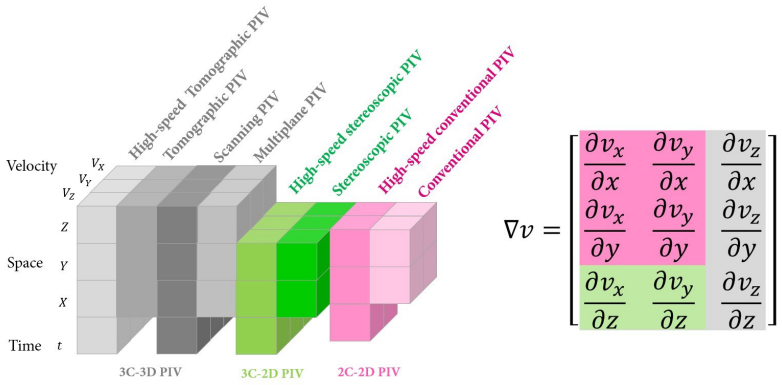

Figure 5: On the left, all different types of PIV techniques are classified based on the number of velocity components and dimensions measured. The time is acquired by the fact if measurements are performed at a single time step or in a complete sequence. On the right, the corresponding velocity gradient is shown [49].

For this research Tomographic PIV was used to study and analyze the blood flow and this method will be explained in depth in the following section.

2.4 Tomographic Particle Image Velocimetry

Tomographic PIV is a 3D measurement technique which has recently been developed [10]. This technique its approach is to discretize the measurement volume containing the particle distribution (the object) as a 3D array of cubic voxel elements with intensity E(X,Y,Z). A cubic voxel is an element that has a uniform non-zero value inside and zero outside and its size is chosen to be comparable to that of a pixel. This is done because the particle images need to be properly discretized in the object as it is done in the images. Furthermore, the integration uses cross-correlation to extend from a pixel to a voxel based object. Then the projection of the light intensity distribution E(X,Y,Z) onto an image pixel (xi,yi) returns the pixel intensity I(xi,yi) which is known from the recorded images. The recorded pixel intensity is the object intensity E(X,Y,Z) integrated along the corresponding line of sight. The 3D intensity distribution E(X,Y,Z) can thus be reconstructed through algebraic reconstruction. The algebraic method thus solves a linear equation linking the pixel intensity $I(x_i, y_i)$ in the image space to the 3D object space which is shown below [49] [50] [51].

$$\sum_{j \varepsilon N_i} w_{i,j} E(X_j, Y_j, Z_j) = I(x_i, y_j) \tag{11}$$

where N_i indicates the voxels that are intercepted or in the neighborhood of the line of sight corresponding to the i_{th} pixel (x_i, y_i) (shaded voxels in figure 6). The weighting coefficient $w_{i,j}$ describes the contribution of the j_{th} voxel with intensity $E(X_j, Y_j, Z_j)$ to the pixel intensity $I(x_i, y_i)$. The weighting coefficients depend on the relative size of a voxel to a pixel and are related to the distance between the voxel center and the line of sight (distance d in figure 6).
Note that $0 \leqslant \mathrm{w}_{i,j} \leqslant 1$ for all voxels.

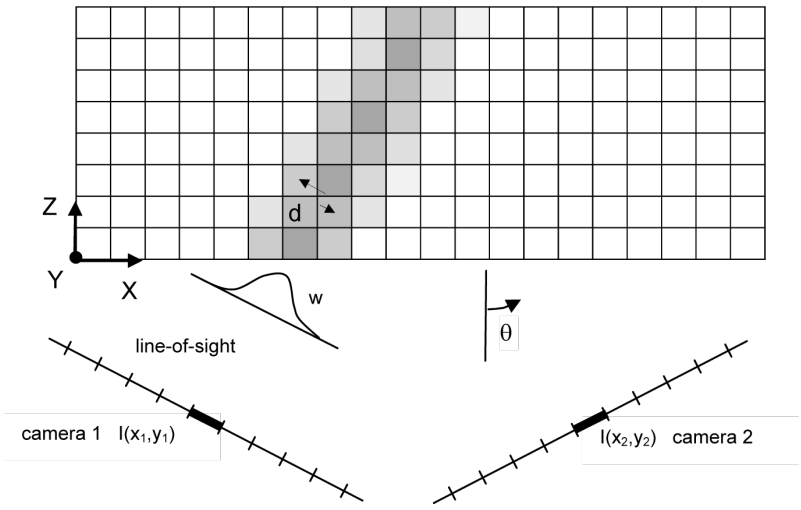

Figure 6: Representation of the imaging model that is used for tomographic reconstruction. In this top-view the image plane is shown as a line of pixel elements and the measurement volume is a 2D array of voxels. The gray level indicates the value of the weighting coefficient $w_{i,j}$ in each of the voxels with respect to the pixel $I(x_1, y_1)$ [52].

3 Material and Methods

The whole process of this research is schematically shown in the flow chart below. For our thesis the data that already was processed in DaVis (Step 2) was received. However, for completeness the whole process is globally explained and the parts done ourselves will be explained in depth (Step 3,4,5).

Figure 7: Visualization of the whole research process.

3.1 Experimental Setup

In the following section is the process of design for the external set-up which contains the aneurysm model and the optical system described. The aneurysm model is manufactured according to identified specifications. In addition, in this sector is the method of how the pump system is built from scratch. The pump system that is created tries to imitate as accurate as possible the pulsating flow that is flowing through an aneurysm.

3.1.1 Phantom

As explained in chapter 2.2.2 there are two dimensionless numbers which characterize the biomedical flow in an aneurysm. These are the Womersley number and the Reynolds number. The Reynolds number oscillates during a cardiac cycle while the Womersley number remains constant. both of these numbers depend on the fluid and the dimensions of the fluid its surroundings. When creating the phantom these two numbers need to be taken into consideration to create dynamic similarity. For PIV to be possible it needs the phantom and working fluid to be transparent so the tracer particles in the fluid can be observed by the camera. In order to create a phantom which is transparent and which can achieve the above mentioned dynamic similarity a lot of materials are not well suited. A second important constraint on the phantom and the working fluid is that the refractive index of the phantom should be the same as the refractive index of the working fluid. If those refractive indices would not be equal there would be optical refraction which would greatly complicate the calculations in processing the pictures. Furthermore, for choosing the phantom material more factors come into play like the working time. Aswin [53] studied the properties of three different PDMS materials for the creation of the phantom. The results are shown in table 1. For our experiment the phantom was made out of the material RTV615 as it has a workable refractive index, not to expensive and also a long working time [24].

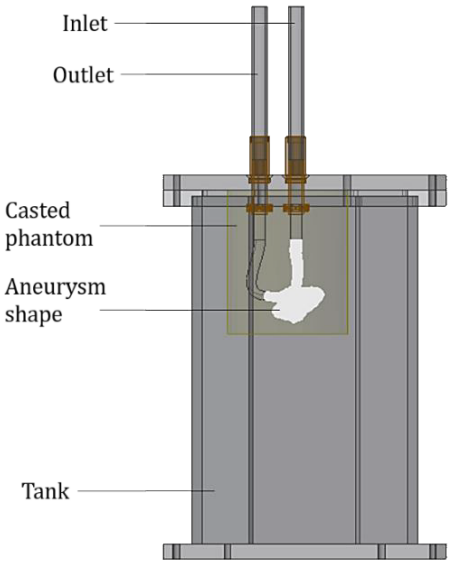

Figure 8: The phantom schematically shown with the model shape in it.

Table 1: Properties of different PDMS materials [53]

Model	**RTV615**	**Sylgard 184**	**EI-1184**
Refractive index	1.406	1.4118	1.42
Working time at 25 °C	4 h	48 h	24 min
Price (€/kg)	57.07	119.66	55.2

3.1.2 Working Fluid

As explained in the previous subsection about the phantom, the working fluid should be transparent and have the same refractive index as the phantom material RTV615. In this research, the working fluid is a water-glycerol solution which is a Newtonian fluid. By changing the ratio of water and glycerol, the refractive index can range from 1.311 (only water) to 1.459 (only glycerol) [49]. This means that the water-glycerol solution can have the same refractive index as the refractive index of RTV615 which is 1.406. Consequently, the density and viscosity of the working fluid are also influenced by matching the refractive indices. This needs to be taken into account because the Reynolds number and Womersly number depend on both the viscosity and density. It is key to first match the refractive index of the working fluid and the material of the phantom and afterwards the dimensionless numbers are matched by altering the dimensions of the phantom and the time of a cardiac cycle.

3.1.3 Setup

The experimental set-up consist of two parts, The flow loop and the optical equipment. The design and control of the flow loop is schematically shown in figure 9. All of these components are needed to recreate the pulsating flow of a cardiac cycle. The used components and their manufacturer are listed in appendix 1.

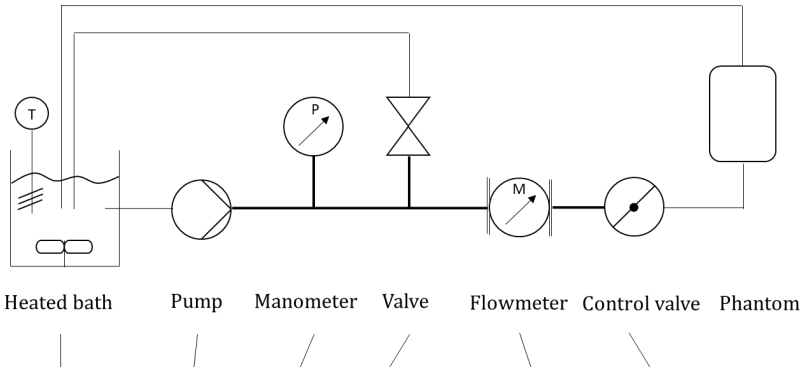

Figure 9: All implemented components to create the set-up are schematically shown.

For capturing the flow two high speed CMOS cameras, two mirrors and a laser are needed. The tomographic PIV set-up that was used is schematically shown in figure 10. Before measurements could be done a lot of calibrating and testing needs to happen to ensure that the measurements would have the least amount of error as possible. When trying to achieve dynamic similarity it is key that the maximum and minimum Reynolds number and the Womersley number are kept constant. When creating the aneurysm scaled model with in mind what was mentioned above a cardiac cycle of 5.1 seconds is found using equation and 3 and equation 4.

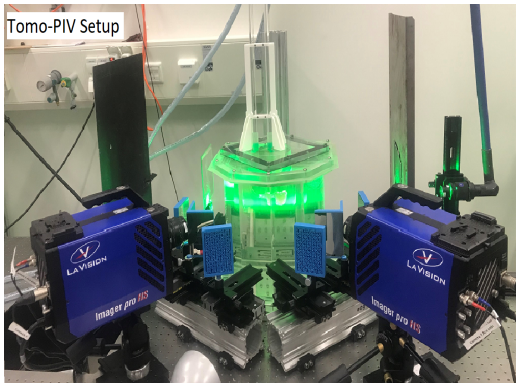

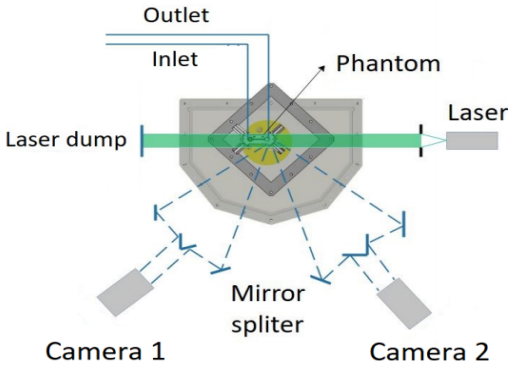

Figure 10: a) The optical setup of Tomo-PIV b) Top view on model and tank with the additional configuration of the cameras, mirrors and the laser (all optical rays arrive perpendicular at the surface of the phantom).

3.2 Post-Processing in DaVis

At this moment the experiment is completed and the pictures are captured and are ready to post-process. For this experiment the whole cardiac cycle of 5.1 seconds was captured in 2040 pictures. This implies that the time between two consecutive pictures is $t = 0.0025$ s. All these pictures are post-processed on the computer. This part of the experiment is crucial to extract useful data out of the pictures. To accomplish this the software DaVis was used. DaVis (computing software LaVision) is software which has a broad applicability. In SPIV and TPIV all the processing, calibration and self-calibration procedures are performed using DaVis [54]. Furthermore, DaVis is also used to trigger the optical system in the steady state part of the research. For the unsteady state part LabView is used as trigger and DaVis is used to approximate the wall of the aneurysm and to perform the vector calculation [55]. After processing the pictures through DaVis it creates data files which contain the location (x, y, z) $[mm]$ and velocity (v_x, v_y, v_z) $[m/s]$ of the particles inside the aneurysm, the time of the picture and a new variable called IsValid which is a variable approximation of the boundary of the aneurysm. IsValid is set to be one, if a non-zero vector exists on the location and is set to be zero if there is no vector. Due to the binary nature of this parameter, this will result in the wall being rough and discrete. Thus, the calculation of the wall shear stress is based on a vector perpendicular to the wall. A parameter study on this parameter from 0.1 to 1 gives a maximum wall shear stress at IsValid=0.5 [24], which is chosen in this research for the wall shear stress calculation. The smoothing procedure of this parameter is given in the next section.

3.3 Tecplot

After processing, DaVis has created for every picture a data file. Every data file can be seen as a time point inside the cardiac cycle. For the research on the aneurysm not all 2040 data points need to be utilized and post processed. The dynamics of a cardiac cycle can be simulated using less timepoints that are evenly spaced throughout the whole cardiac cycle. Using this the TAWSS, OSI and Trans-WSS can be calculated for different amounts of timesteps. This is done for multiple reasons like decreasing computation time or saving computational power. In the results the different amount of timesteps to calculate the TAWSS, OSI and Trans-WSS are explained in more detail. Before loading the Binary data files created by DaVis into the next step it is convenient to convert these files to another type of file. This is key for decreasing loading time and thus increasing the work convenience. A macro was created in which Tecplot can convert these data files in sequence. This script with explanation can be found in appendix 2. When loading these converted data files into Tecplot it can create a useful image of the aneurysm and it can be altered to create the images below.

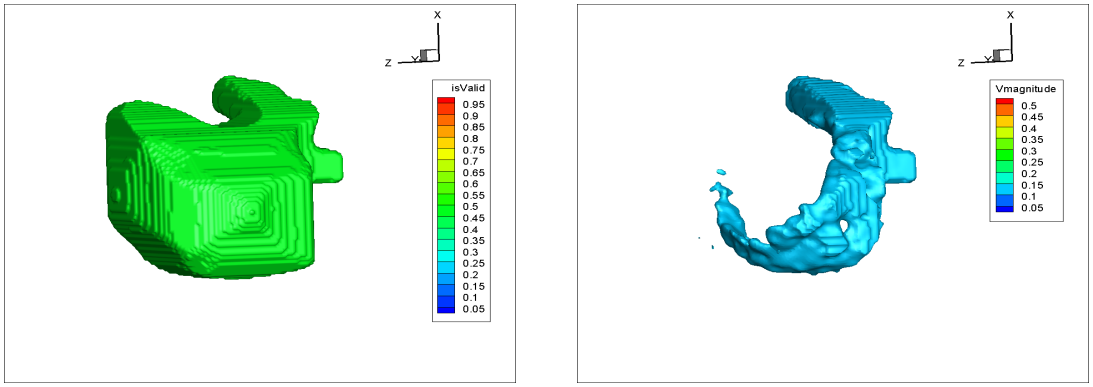

(a) A visualization of the Aneurysm with contour of IsValid (Boundary approximation)

(b) $V_{magnitude}$ shown for values higher then 0.13 m/s (t=2.2825)

Figure 11: In image (a) the aneurysm wall approximation from DaVis is visualized. in image (b) the magnitude of the velocity is shown for values higher then 0.13 m/s.

As can be seen in image 11 Tecplot is a very powerful program which has a lot of functions incorporated. To be able to calculate the TAWSS, OSI and the Trans-WSS the wall shear stress needs to be calculated and therefor the velocity components are needed. To run these calculations in sequence for multiple data points a macro needs to be created. A macro is some kind of script in which commands are stored. This is very convenient because Tecplot can run these macros and this makes it achievable to perform repeating steps for large datasets. The macro that was created and used in this thesis can be found in appendix 3 and the commands that are used in this script are explained hereafter.

The data is loaded into Tecplot and the variables needs to be altered so that they are all noted in SI-units. Furthermore, the axis need to be defined to the Cartesian coordinate system in SI-units and after that the speed can be calculated with the following formula.

$$V_{magnitude} = \sqrt{V_x^2 + V_y^2 + V_z^2} \ [\frac{m}{s}] \tag{12}$$

The velocity magnitude is calculated and shown in Tecplot and can now be used to better understand how the blood flows through the aneurysm. The stream traces of the velocity for three different times in the cardiac cycle are shown in image 12.

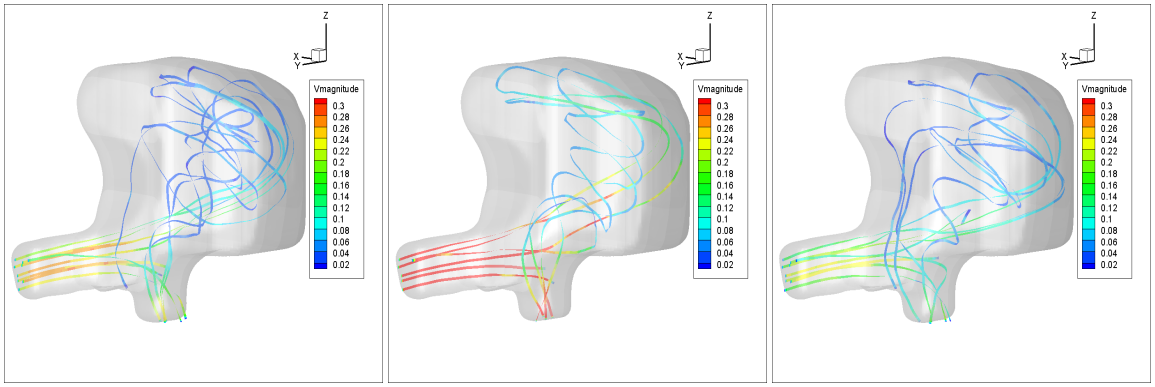

(a) t = 0.6 sec (begin cardiac cycle)

(b) t = 2.3 sec (middle cardiac cycle)

(c) t = 4.8 sec (ending cardiac cycle)

Figure 12: In this image $V_{magnitude}$ stream traces shown for three time points in the cardiac cycle (Outlet is pointed downwards, inlet is pointed in the screen).

When the field variables are correctly assigned an implemented function in Tecplot can be used which calculates the velocity gradient for all points in time. All these steps that have been made apply to all the datasets that were loaded into the Tecplot frame. The next two steps apply only to one zone which in our case is one dataset and thus one timepoint. Firstly, the Isvalid surface is smoothed with the smooth function in Tecplot. Secondly, the Iso-surface is extracted which creates a new empty zone. Afterwards, Linear interpolating is done to extract the data to the new zone. To run these two steps in batch mode a for-loop can be created in the macro.

When this is done for all loaded frames the grid K unit normal can be calculated. The Grid K Unit Normal is meaningful for both structured and unstructured grids. For structured grids it is the normal in the positive K-direction. For unstructured grids as our aneurysm it is the normal for surface cells (triangles quads) in the direction determined by the right-hand rule. In our case will this result in a vector that points inwards from the aneurysm surface. When the calculations have finished we can calculate the magnitude of the WSS for all locations at each time [56]. The preceding equations can be found in appendix 4.

$$\tau = \sqrt{(\overrightarrow{\tau_x})^2 + (\overrightarrow{\tau_y})^2 + (\overrightarrow{\tau_z})^2} \ [Pa] \tag{13}$$

The Wall shear stress is calculated for all points in space and for all time points and with this a better insight into the aneurysm and its flow characteristics can be found. $\overrightarrow{\tau_x}, \overrightarrow{\tau_y}, \overrightarrow{\tau_z}$ are the summations of all tau components in the x, y, z direction. The components that are summed to create these tau components are schematically shown in the figure below.

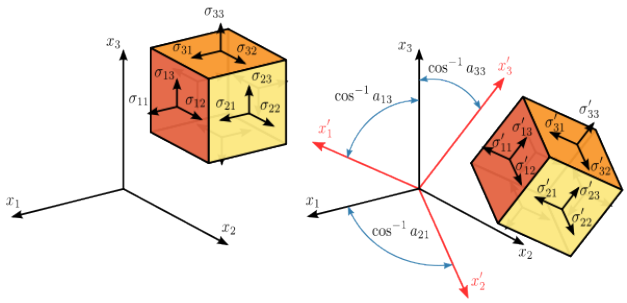

Figure 13: Stress tensor shown for a cube in 3D. In this research $\sigma_{x,y,z} = \tau_{x,y,z}$.

The next step is calculating the hemodynamic quantities. Unfortunately, Tecplot lacks the ability to do this due to the fact that the implemented integration techniques in Tecplot are not applicable. Therefore a new approach needs to be found and this means this was the last step that is implemented in the macro script. Fortunately, there is another function in Tecplot which can be used. It is possible to link Python with Tecplot which opens new opportunities. Python is a language which is widely used around the world. This type of code makes working with arrays, matrices and all sorts of data much more applicable. To use Python with Tecplot it needs to be set-up so that it can allow live connections with command prompt. When this is done correctly the next step is extracting the variables which are needed for the calculation. These variables are $x, y, z, \tau, \overrightarrow{\tau}_x, \overrightarrow{\tau}_y, \overrightarrow{\tau}_z$, The K-grid and the solution time. Using Python and its capabilities for array summation it is possible to add the variables together to calculate the TAWSS, OSI and the Trans-WSS using equations 6, 7 and 8 stated in section 2.2.4. When this is completed the newly calculated variables need to be imported back into Tecplot so a visualization can be made. The python script which was used to finalize this report is added in the appendix and can be found in section 5.

4 Results

In this chapter the results for the obtained Wall Shear Stress, Time-Averaged Wall Shear Stress, Oscillatory Shear Index and Transverse Wall Shear Stress are displayed using the experimental set-up and method explained in the previous chapter. Firstly, some WSS results are shown at specific timepoints during the cardiac cycle. Secondly, The TAWSS, OSI and Trans-WSS are calculated using a different amount of time steps that are evenly spaced in the cardiac cycle as explained in section 3.3. The results for the TAWSS, OSI and Trans-WSS are shown for 11, 21, 51 and 101 timepoints. These amounts of timepoints are chosen because the resulting TAWSS, OSI and Trans-WSS can indicate the influence of the accuracy of the results when increasing the amount of timepoints. The specifications of these amounts of timepoints are shown in table 2.

Table 2: The specifications shown for 11, 21, 51 and 101 evenly spaced timepoints during the whole cardiac cycle.

Number of timepoints	Number of points between adjacent timepoints	Difference in time between adjacent timepoints [s]
11	204	0.51
21	102	0.255
51	40	0.1
101	20	0.05

4.1 Wall shear stress

First some results of the magnitude of the Wall Shear Stress during the cardiac cycle are presented to exhibit how the magnitude of the WSS on the aneurysmal wall changes during the cardiac cycle. For these figures a smoothness ratio was needed to be found so a realistic image could be created. Using trial and error and calculating the magnitude of the WSS for different amounts of smoothness it was found that smoothing for 20 times gave the best results. The magnitude of the WSS is shown on times 0.1 s, 1.1 s, 2.1 s, 3.1 s, 4.1 s and 5.1 s in figure 14. In this figure, the result of the cardiac cycle can be seen clearly. At the start of the cardiac cycle (t = 0.1 s) is the magnitude of the WSS over the whole surface low and starts to increase. The magnitude of the WSS peaks between 2.1 s and 3.1 s and then reduces up until 5.1 s. It can be seen that the magnitude of the WSS at 0.1 s and 5.1 s are very similar which is logical as the end of one cardiac cycle is the beginning of the next cardiac cycle. Furthermore, When looking at the figures it can be seen that near the inlet and outlet of the aneurysm the magnitude of the WSS is the highest. This is what is expected because the magnitude of the WSS is related to the magnitude of the velocity which shows similar patterns.

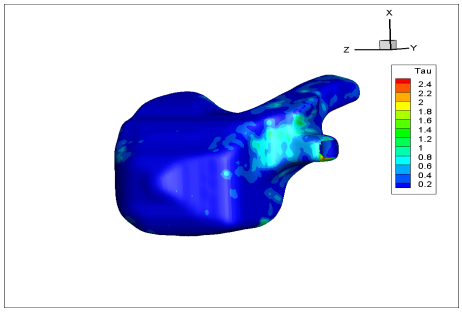

(a) The magnitude of the WSS is shown as a contour on the aneurysm at time t=0.1.

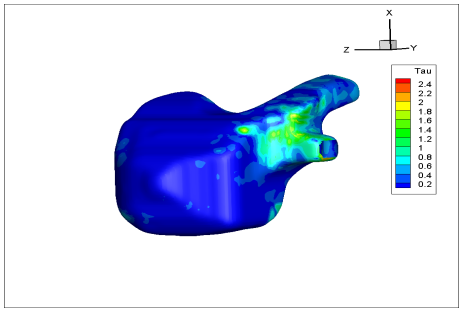

(b) The magnitude of the WSS is shown as a contour on the aneurysm at time t=1.1.

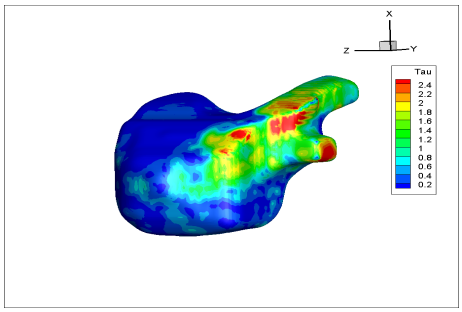

(c) The magnitude of the WSS is shown as a contour on the aneurysm at time t=2.1.

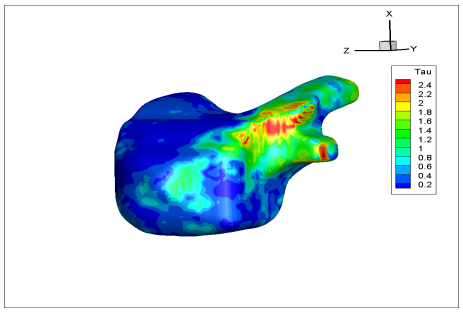

(d) The magnitude of the WSS is shown as a contour on the aneurysm at time t=3.1.

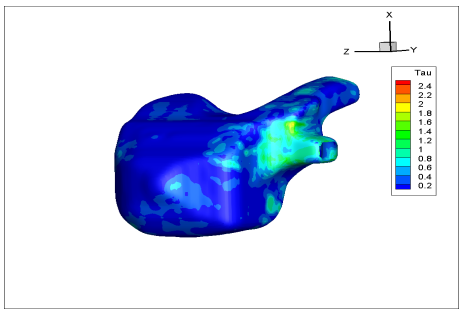

(e) The magnitude of the WSS is shown as a contour on the aneurysm at time t=4.1.

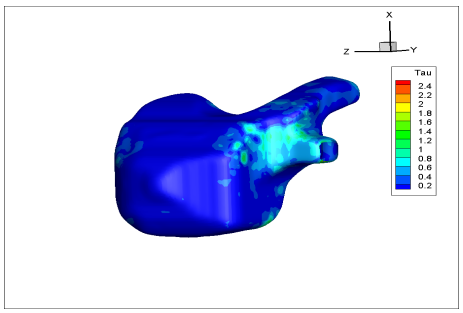

(f) The magnitude of the WSS is shown as a contour on the aneurysm at time t=5.1.

Figure 14: In this image the magnitude of the magnitude of the WSS is projected onto the aneurysm surface for different time steps which form the whole cardiac cycle.

4.2 Time averaged wall shear stress

The Time averaged Wall Shear Stress (TAWSS) is computed for every point on the boundary of the aneurysm using equation 6 in Python and Tecplot. The calculations for the TAWSS are done for 11, 21, 51 and 101 timepoints and these plots are visualised in figure 15.

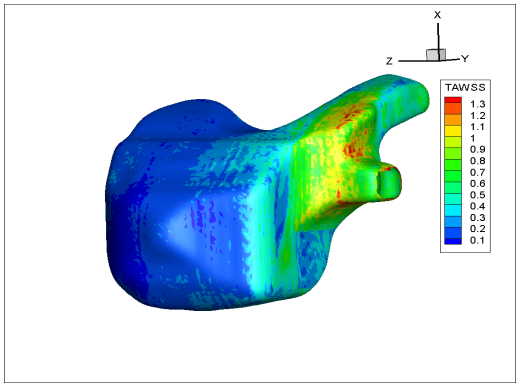

(a) The TAWSS is shown as contour on the aneurysm calculated for 11 timepoints.

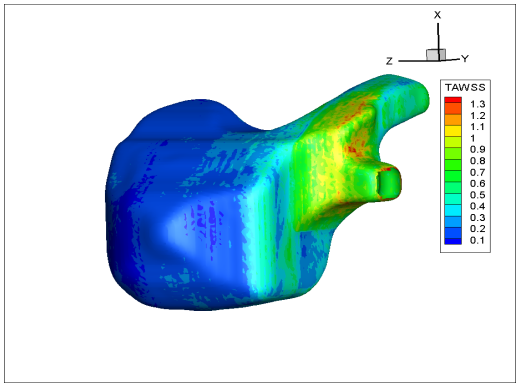

(b) The TAWSS is shown as contour on the aneurysm calculated for 21 timepoints.

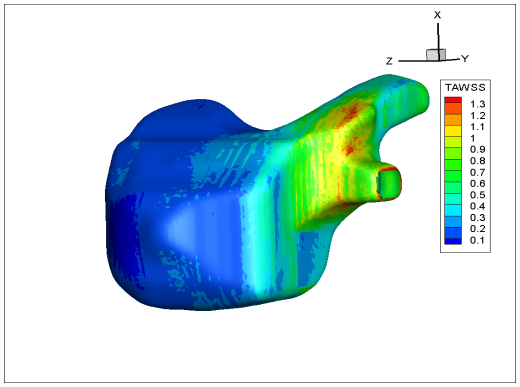

(c) The TAWSS is shown as contour on the aneurysm calculated for 51 timepoints

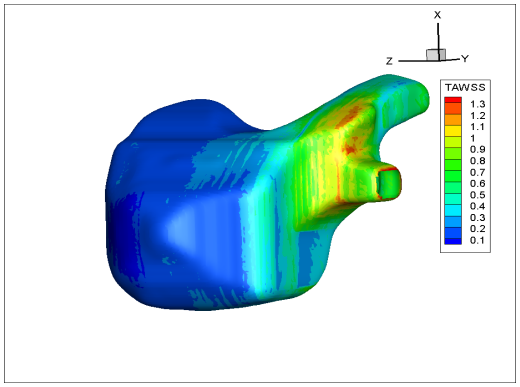

(d) The TAWSS is shown as contour on the aneurysm calculated for 101 timepoints.

Figure 15: In this image the TAWSS, calculated over the whole cardiac cycle, is projected onto the surface of the aneurysm for different amounts of time steps in between.

From these plots it is clearly visible that the TAWSS stays more or less the same when changing the amount of time points in a cardiac cycle that are implemented into the calculations. However, there are some minor differences when the total amount of timepoints is increased. When comparing image 15a with image 15d it can be seen that image 15d is much more smooth and this is expected when increasing the data points in calculating the TAWSS. When comparing plot 15c with plot 15d it is clear that the differences in smoothness become rather small which concludes that increasing the data points will not keep increasing the smoothness of the images. Therefore, not more then 51 data points are needed.

Furthermore, when looking at the TAWSS it can be seen that the high values can be found at the inlet and outlet of the aneurysm. As the TAWSS is the average of the WSS during the cardiac cycle, the high values of TAWSS near the inlet and outlet of the aneurysm are a direct result of high magnitudes of the WSS near the inlet and outlet during the cardiac cycle. The high magnitudes of the WSS near the inlet and outlet during the cardiac cycle can be seen in figure 14.

4.3 Oscillatory shear index

As described in section 2.2.4, the Oscillatory shear index (OSI) can be calculated using equation 7. The OSI is an index that can be seen as the disturbance in direction of the WSS. In figure 16 is the OSI visualized onto the aneurysm wall for 11, 21, 51 and 101 timepoints during a cardiac cycle.

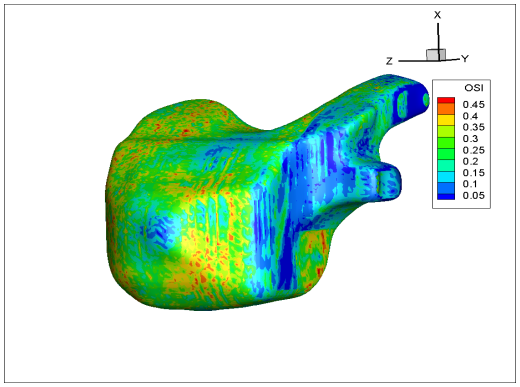

(a) The OSI is shown as contour on the aneurysm calculated for 11 timepoints.

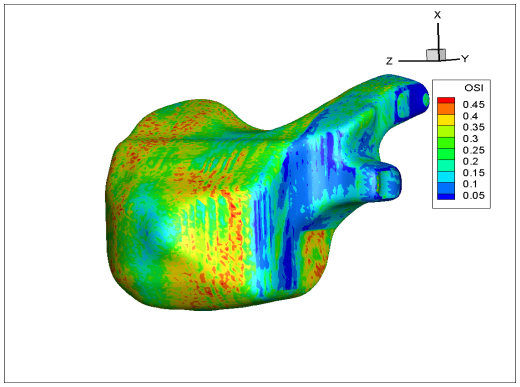

(b) The OSI is shown as contour on the aneurysm calculated for 21 timepoints.

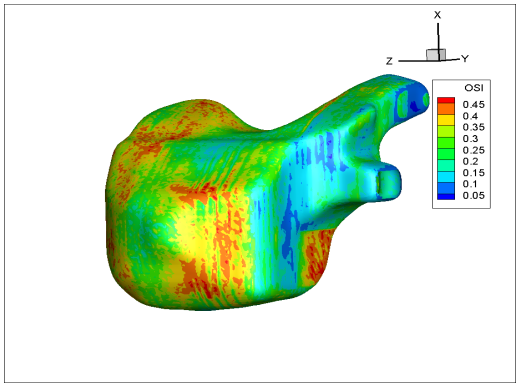

(c) The OSI is shown as contour on the aneurysm calculated for 51 timepoints.

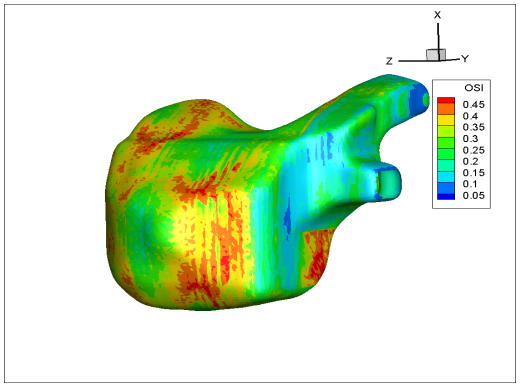

(d) The OSI is shown as contour on the aneurysm calculated for 101 timepoints.

Figure 16: In this image the OSI, calculated over the whole cardiac cycle, is projected onto the surface of the aneurysm for different amounts of time steps in between.

The areas of high OSI indicate regions of high variability of the WSS. The areas of low OSI indicate regions where the WSS is approximately always moving in one direction. From the plots it is clear that the OSI becomes a lot smoother when increasing the number of timepoints. This is a logical result because when the amount of data points throughout the whole cardiac cycle is increased more local fluctuations of the wall shear stress are taken into account. In the same logic, the largest differences can be seen when comparing the plot of 11 timepoints and the plot of 101 timepoints. It can also be seen that the values of the OSI at the inlet and outlet are between large and small. This can be explained by two facts. Firstly, the flow of blood at the inlet and outlet is mostly moving in one direction so a very large value of the OSI is not expected. Secondly, the

flow can not be perfectly uniaxial as there is still an aneurysm where blood flows in and out which influences the blood stream in the artery.

In addition, in plot 16a there are only very small regions of high OSI. These regions become slightly bigger in plot 16b but the biggest difference in the size of these areas are between plot 16b and 16c. Between 51 and 101 timepoints in respectively plots 16c and 16d these areas appear to remain unchanged. In conclusion, for a good calculation of the OSI on the aneurysm, a minimal of 51 evenly spaced timepoints are needed during the cardiac cycle. However, this is only done when computational power and time management are an issue. When this is not the case adding more data points will produce a more accurate result due to the fact that more local fluctuations during a cardiac cycle will be taken into account.

4.4 Transverse WSS

As described in section 2.2.4 the Transverse Wall Shear Stress (Trans-WSS) can be calculated using equation 8. The Trans-WSS has the property to distinguish between uniaxial pulsatile flow and multidirectional flow. The Trans-WSS is visualized onto the aneurysm wall for 11, 21, 51 and 101 timepoints during a cardiac cycle and is shown in figure 17.

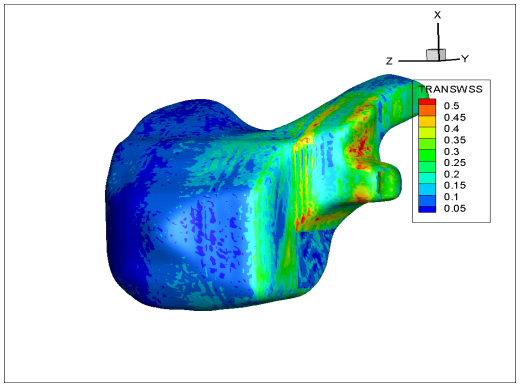

(a) The Trans-WSS is shown as contour on the aneurysm calculated for 11 timepoints.

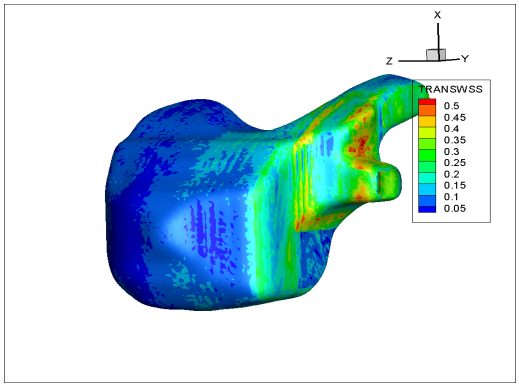

(b) The Trans-WSS is shown as contour on the aneurysm calculated for 21 timepoints.

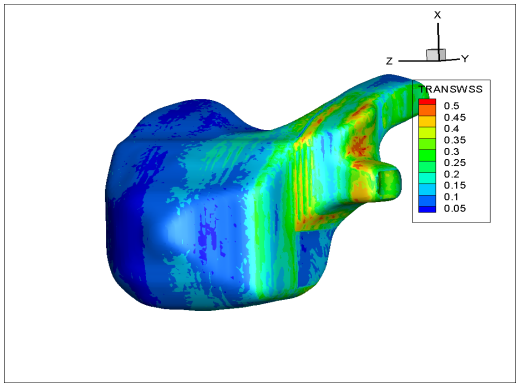

(c) The Trans-WSS is shown as contour on the aneurysm calculated for 51 timepoints.

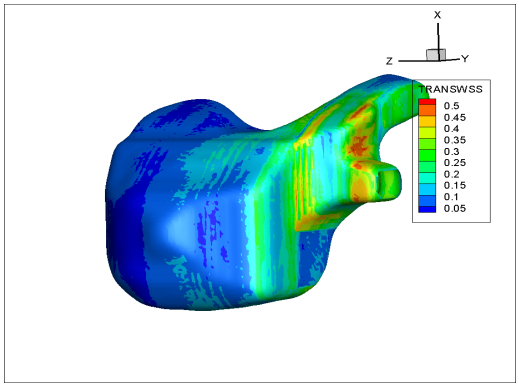

(d) The Trans-WSS is shown as contour on the aneurysm calculated for 101 timepoints.

Figure 17: In this image the Trans-WSS, calculated over the whole cardiac cycle, is projected onto the surface of the aneurysm for different amount of time steps in between.

First thing to notice when looking at all the sub-figures in figure 17 is that the figures are very similar. It can be concluded that adding more time points in between and thus increasing the computing time does not increase the validity of the measurements. However adding more time points does give a smoother result.

The Trans-WSS has a bounded regime due to the nature of its calculation. The Trans-WSS can take any value from 0 to the value of the TAWSS. When the Trans-WSS is low as in the back of the bulge of the aneurysm this indicates that the direction of the WSS remains approximately parallel along to a single axis throughout the cardiac cycle. However, when looking just after the inlet of the aneurysm, a High trans-WSS can be seen which accounts for large changes in the direction of the WSS. This is also what is expected due to the fact that just after the inlet the flow is disturbed by the flow out of the aneurysm and thus becomes very volatile. As mentioned before the Trans-WSS does not completely characterize the dynamics of the Wall Shear Stress. It cannot distinguish between a unidirectional flow and a reversing but uniaxial flow. When comparing these images with the images of the OSI in figure 16 it can be seen that on location where the Trans-WSS is low a high OSI can be found and vice versa. When comparing the equation of the OSI (7) and of the Trans-WSS (8) this could be because considering the main wall shear stress term can be found in both equation only to be each others inverse. Not many literature results can be found on this newly reintroduced hemodynamic quantity. Although, the situation in every aneurysm is different it can be used to compare and check the results for validity. in a research on the lipoprotein transport in a rabbit aorta and its correlation with atherosclerotic plaque thickness was studied [9]. In this study the Trans-WSS was calculated for this artery. When looking at the results some similarities can be found with our figures. Firstly, it can be seen that the domain of both Trans-WSS are compatible. Secondly, the Aneurysm that was researched has a bend between the inlet and outlet. In this bend the highest Trans-WSS can be found. For the rabbit aorta this was also concluded.

4.5 Region Comparing

In this section the different regions of an aneurysm will be considered. All the hemodynamic quantities are revisited and compared. In figure 18 is the magnitude of the WSS shown together with the TAWSS, OSI and Trans-WSS calculated using 51 timepoints.

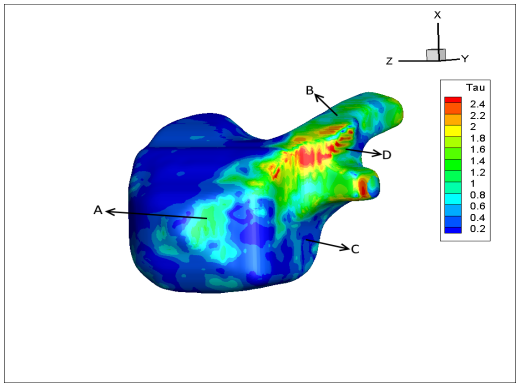

(a) The WSS shown with a indications of the different regions that will be compared (t=3.1 sec).

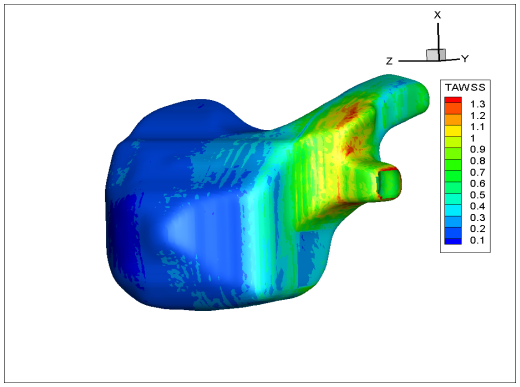

(b) The TAWSS is shown as contour on the aneurysm calculated for 51 timepoints.

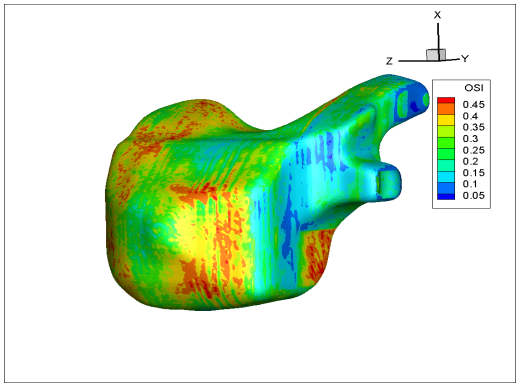

(c) The OSI is shown as contour on the aneurysm calculated for 51 timepoints.

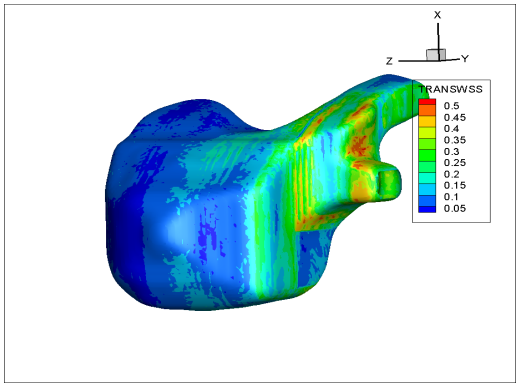

(d) The Trans-WSS is shown as contour on the aneurysm calculated for 51 timepoints.

Figure 18: In the image 18a are the comparing regions shown. In image 18b,18c and 18d are all the hemodynamic quantities shown for 51 timepoints.

Generally speaking, regions with low WSS and low TAWSS tended to have high OSI or Trans-WSS. For instance region A has a low WSS and also a very low TAWSS and a high OSI. As described in 2.2.4 this low TAWSS and high OSI could result in enlargement of the aneurysm and possibly rupture. When looking at the hemodynamic quantities in region B something peculiar is noticed. All four hemodynamic quantities are neither high or low. This can be explained due to the fact that this is the inlet where the flow and the WSS vary a lot during the whole cardiac cycle. Furthermore, it can be seen that in region C a high OSI can be found while the TAWSS and the magnitude of the WSS in the middle of the cardiac cycle are very low. When looking at region D it can be seen that the Trans-WSS is the highest as is the WSS and the TAWSS. This is due to the fact that this is between the inlet and outlet where the flows direction fluctuates a lot and also a high fluctuating velocity magnitude occurs.

5 Discussion

5.1 Blood as a Newtonian fluid

In this thesis the blood and its components are assumed to be a Newtonian fluid as described in section 2.2. This assumption is based on the fact that the viscosity of blood is approximately constant when the shear rate is above 100 s^{-1}. When the shear rates are lower than 100 s^{-1} the blood cells will bond together and form aggregates. When the shear rate decreases further this will also lower the amount of aggregates and at the same moment will their size increase which exponentially increases the viscosity of the blood [19]. When blood is assumed to be a Newtonian fluid this will simplify the calculation of the WSS because the WSS becomes linear with the wall shear rate. Razavi et al [20] stated that in the circle of Willis is the wall shear rate higher than 100 s^{-1} during the whole cycle which is in agreement with the recent results reported by Alimi [57]. Alimi found that the shear rate is in a large part of the circle of Willis higher than 100 s^{-1}. The exception where the shear rate is lower are some of the bifurcations of the circle of Willis. Consequently, it is a valid approximating to assume during the whole cardiac cycle that the blood in the artery is a Newtonian fluid. However, Xiang et al. [58] found that the wall shear rate in an aneurysm is overestimated using the Newtonian model for the blood viscosity. This approximation contributes thus an error to the calculation of all hemodynamic quantities calculated in this research. For further research it is recommended to use the Carreau-Yasuda or the Casson model [19]. This will resolve a part of the non-Newtonian behavior of blood. Unfortunately, to this date no model is known that can fully capture the whole behavior of the bloods viscosity.

5.2 Approximation of the integrals

For this research a lot of calculations were done involving multiple integrations. The data for this research was gathered using Tomographic-PIV which created data in the discrete time domain. Integrating over discrete time is not possible thus one of the Quadrature rules based on interpolations was used (midpoint/rectangle rule). This rule is an assumption and the accuracy relies on the width of the time interval between two summed values and also does the volatility of the integrated quantity play a role. In the case of our research this width of the time interval between two data points was very small and the error resulting from this approximation could be almost negligible when all the data points were used. However, the amount of data that was able to be post processed was limited by the computation power of the computer. To decrease this error in future experiments the computer could be improved so that more data could be post processed which would decreases the width of the time interval between summed values and thus decreasing the error in the assumption.

5.3 Dynamic similarity using the Reynolds and Womersley number

In acquiring dynamic similarity between the flow inside an actual aneurysm and inside the phantom, the Reynolds and Womersley number of the flow in an actual artery are matched to the Reynolds and Womersley number for the the phantom as explained in section 2.2.2. When assuming blood as a Newtonian fluid the Womersley number remains constant during the cardiac cycle. The Reynolds number depends on the speed of the blood in the artery so the value of the Reynolds number varies during a cardiac cycle. The flow in a real artery is abrupt due to the sudden contractions of the heart atria and ventricles and therefor hard to simulate. As a result, matching the Reynolds number of the phantom to the Reynolds number of the blood in the real artery during the whole cardiac cycle is extremely difficult [24].

Accordingly, these assumption on the Reynolds and Womersley number result in the Reynolds and the Womersley number for the flow in the phantom not being equal to the Reynolds and the Womersley number for the flow inside the real artery, so the flow characteristics differ and perfect dynamic similarity is not achieved. As the characteristics of the flow differ an additional error is added to the calculation of the hemodynamic quantities. This error increases more when the non-Newtonian behavior of the blood is also taken into account. In further research to reduce the error two things need to happen. First, the Reynolds number needs to be accurately simulated so the cardiac cycle in the phantom resembles the cardiac cycle in the aneurysm. Secondly, the non-Newtonian behavior of the blood needs to be accounted for. When this is implemented it must be considered that the Womersley number and Reynolds number will also change due to the non-Newtonian behavior of the fluid.

5.4 Data transfers

A lot of different programs and applications were used from the beginning of the research until the post processing of the data. The research started with measuring using LabView and then subsequently DaVis was used. The biggest part of post processing happened in Tecplot in combination with Python. Every program and application has its strengths and flaws and they all contribute in the accuracy of the results of this research.

LabView was used to trigger the cameras and does a good accurate job. Not much of an error was mentioned by our predecessors in this part of the research [55].

DaVis has multiple ways to create useful data out of the pictures. Some settings greatly decrease the computing time at the expense of the accuracy of the data gathered from the pictures of the aneurysm. These settings result in a less smoother and less realistic representation of the aneurysm after interpolation. Unfortunately, we do not know which settings were used to interpolate the data in DaVis so not much can be said about the error contribution of this step.

Afterwards, The interpolated data is imported into Tecplot. This step has no error contribution. However, when extracting the data into python and reinserting it into Tecplot this could create some rounding difference which could contribute to the error. However, this error is neglectable small and was only mentioned for completeness.

Concluding, every program and application has its strengths and weaknesses and the operation of multiple programs can have a lot of benefits. The important thing is that the integration of multiple programs needs to be done precisely and thorough. This can be achieved with two solutions. Solution one is decreasing the amount of times migration between programs take place. Solution two is increasing the amount of information that is available over the research. This is to prevent data from being mishandled due to lack of information or capabilities by researchers at different parts of the process. In addition, if the research information for every step of the process could be increased and better noted this would create an easy hand over between researchers in different steps of the process which avoids miscommunication and consequently mishandling of the data.

5.5 Tomographic PIV measurements

This research was conducted using one dataset of 2040 pictures which resembled a whole cardiac cycle inside an aneurysm. These pictures were taken using a Tomographic set-up and these measurements were done for one cardiac cycle. However, this approach is sensitive for errors in the measurements. If there would be a random error or systematic error it would not be exposed and would cloud the dataset. This type of error can be decreased by conducting follow-up measurements and creating multiple datasets of multiple cardiac cycles. Averaging over all these measurements and its results will create a more stable dataset which is less sensitive for errors in the measurements. My recommendation is to increase the amount of follow up measurements and averaging the final results to create a more stable result.

5.6 Python

For this research Python coding was needed to calculate the advanced hemodynamic quantities. Learning the language Python as for the Tecplot macro language in ten weeks time is a difficult job especially when considering that this time would already be a short period to conduct a full research. Time-management was always a struggle in this research and I believe we have done very well in this part. However, due to the constraints in time some consents were made. One of these consents was part of the way the code handles the data. When summing the data from a quantity over time which was needed for the TAWSS, OSI and the Trans-WSS a consent in the calculation was made. The code was built for a data set with a constant structure in the Cartesian coordinates. This was not the case as the data structure in this research was not consistent. For example, the first row at time 1 for a variable could be about location $x = 0.5, y = 0.5, z = 0$ and at the second time the first row could be about $x = 0.5, y = 0.5, z = 0.5$ which when summed creates an inaccuracy. I believe this consent is the cause for the contour images not being smooth and showing lines instead of stains. The reason why the stripes are vertical in the y,x plane is due to the fact that Tecplot sorts the data in the sequence: y,x,z. This error was foreseen but requires advanced coding or different type of data structure to avoid. For further research I would recommend one of these two solutions to remove this inaccuracy. First solution, adding a part of code which filters and automatically sorts the data based on Cartesian coordinates for every time point so data addition is possible. This code can be cumbersome and very tedious to create and would still not completely rule out the error but greatly decrease it. Secondly, another solution which is easier but requires more storage space is to change the data structure DaVis creates. If DaVis is set-up so that the data structure is built for every time point in the same x,y,z coordinate structure the error will be eliminated. More information about the data structure that was used in this research and the data structure it needs to be is added in appendix 6

6 Conclusion and Future Recommendations

In this research the Wall Shear Stress, Time-Averaged Wall Shear Stress, Oscillatory Shear Index and the Transverse Wall Shear stress of an intracranial aneurysm are calculated. The data to calculate these hemodynamic quantities was retrieved from a realistic phantom using Tomographic Particle Image Velocimetry. The research consist out of two parts.

The first part of our research goal was to check to what extent it was possible to retrieve these hemodynamic parameters from the velocity fields of DaVis. All hemodynamic parameters were extracted from the velocity fields and appear to have plausible outcomes. blood is assumed to be a Newtonian fluid and the dynamic similarity between a real artery and the used phantom is not optimal which results in a less realistic model. In addition, minor approximations are made and during post-processing some consents due to time constraints are accepted. It is unknown to what extent these results coincide with real intracranial aneurysms due to these before mentioned contributions.

The second part of our research goal was to research the amount of data time points that were needed to achieve accurate results for these hemo dynamic quantities. These quantities are calculated for different time steps and with these results a conclusion can be made about the amount of timesteps in a cardiac cycle that is necessary to post process to create accurate results. Both of these parts will be considered separately per hemo-dynamic quantity.

The first hemodynamic quantity that was calculated was the Time Averaged Wall Shear Stress (TAWSS). It was found that the TAWSS is low for the bulge of the aneurysm and high near the inlet and outlet. This was expected because during the cardiac cycle the WSS was the highest at the inlet and outlet. Furthermore, to create an accurate result of the TAWSS not more then 51 timepoints were needed during a cardiac cycle.

Secondly, the Oscillating Shear Index (OSI) was calculated. It was found that unlike with the TAWSS the OSI was low near the inlet and outlet and higher in the bulge of the aneurysm. In addition, The OSI is expected to be very dependant on the local fluctuations that happen during a cardiac cycle. It was found that to create an accurate result more then 51 timepoints are needed. While keeping in mind that adding more timepoints increases the accuracy due to the fact that more local fluctuations are taken into account.

Thirdly, the Transverse Wall Shear Stress (Trans-WSS) was calculated. It was found that the Trans-WSS is a rather specific hemo-dynamic quantity as it tries to shed light on the para-axial changes in the flow. It is found that the Trans-WSS was high near the inlet and outlet and low in the bulge of the aneurysm. Furthermore, adding more time points in between gives a smoother image but it remains the same. To create an accurate result not more then 51 time points were needed.

As can be seen in the calculation of the hemodynamic quantity adding more data does not necessarily have to create a more accurate result. What it can do, is shed light on local fluctuations

or create a smoother image. When computing the TAWSS, OSI and Trans-WSS with limited computing power and time it is adequate to work with 51 timepoints in a whole cardiac cycle to extract these hemodynamic parameters.

Unfortunately, not much can be said about the rupture risk of our aneurysm because the location and time of the rupture is unknown. If a phantom is created based on a real aneurysm with a known rupture site, one can check whether these quantities can predict this rupture site using the hemodynamic parameters that were calculated in this research.

For further development of this thesis a lot can be gained by altering the data structure to a rigid Cartesian structure at the beginning of the research process. This makes way for a lot of advantages later on in post processing. The results will become more and smooth. In addition, data management will be more accessible and understandable. On the contrary, more computing power and storage will be needed but I believe the pros outweigh the cons. Furthermore, the Carreau-Yasuda or the Casson model can be implemented to account for the non-Newtonian behavior of blood which was not taken into account in this research

In the far future, the risk assessment of the rupture of an intracranial aneurysm may be conducted by Artificial Intelligence (AI). This AI could learn from every aneurysm and its rupture point. It could try and find the combination of these previously mentioned hemodynamic quantities and consequently will be able to identify when an aneurysm will rupture and also where it will rupture. As a result the AI will be able to do a valid risk assessment on further treatment.

References

[1] Brain Aneurysm Foundation. Brain aneurysm statistics and facts. `https://bafound.org/about-brain-aneurysms/brain-aneurysm-basics/brain-aneurysm-statistics-and-facts/`, September 2019. Visited on 26-06-2020.

[2] N. M. Ajiboye, N. M. Chalouhi, R. M. Starke, M. M. Zanaty, and R. M. Bell. Unruptured cerebral aneurysms: Evaluation and management. *The Scientific World Journal*, 2015:1â10, 2015.

[3] D. M. Nasr and R. D. Brown. Management of unruptured intracranial aneurysms. *Current Cardiology Reports*, 18(9), 2016.

[4] L. N. Williams and R. D. Brown. Management of unruptured intracranial aneurysms. *Neurology: Clinical Practice*, 3(2):99â108, Jan 2013.

[5] W. Brinjikji, Y.-Q. Zhu, G. Lanzino, H.J. Cloft, M.H. Murad, Z. Wang, and D.F. Kallmes. Risk factors for growth of intracranial aneurysms: A systematic review and meta-analysis. *American Journal of Neuroradiology*, 37(4):615â620, 2015.

[6] A. Selimovic, Y. Ventikos, and P. N. Watton. Modelling the evolution of cerebral aneurysms: Biomechanics, mechanobiology and multiscale modelling. *Procedia IUTAM*, 10:396â409, 2014.

[7] H. Meng, V.M. Tutino, J. Xiang, and A. Siddiqui. High wss or low wss? complex interactions of hemodynamics with intracranial aneurysm initiation, growth, and rupture: Toward a unifying hypothesis. *American Journal of Neuroradiology*, 35(7):1254â1262, Jul 2014.

[8] A. L. Dicarlo, D. W. Holdsworth, and T. L. Poepping. Study of the effect of stenosis severity and non-newtonian viscosity on multidirectional wall shear stress and flow disturbances in the carotid artery using particle image velocimetry. *Medical Engineering Physics*, 65:8â23, 2019.

[9] Xiaoyin Li, Xiao Liu, Peng Zhang, Chenglong Feng, Anqiang Sun, Hongyan Kang, Xiaoyan Deng, and Yubo Fan. Numerical simulation of haemodynamics and low-density lipoprotein transport in the rabbit aorta and their correlation with atherosclerotic plaque thickness. *Journal of The Royal Society Interface*, 14(129):20170140, 2017.

[10] Christoph Roloff, Daniel Stucht, Oliver Beuing, and Philipp Berg. Comparison of intracranial aneurysm flow quantification techniques: standard piv vs stereoscopic piv vs tomographic piv vs phase-contrast mri vs cfd. *Journal of NeuroInterventional Surgery*, 11(3):275â282, 2018.

[11] Marcelo Raschi, Fernando Mut, Greg Byrne, Christopher M. Putman, Satoshi Tateshima, Fernando Vinuela, Tetsuya Tanoue, Kazuo Tanishita, and Juan R. Cebral. Cfd and piv analysis of hemodynamics in a growing intracranial aneurysm. *International Journal for Numerical Methods in Biomedical Engineering*, 28(2):214â228, 2011.

[12] M. S. van Kammen, C. J. Moomaw, I. C. van der Schaaf, R. D. Brown, D. Woo, J. P. Broderick, J. S. Mackey, G. J. E. Rinkel, J. Huston, Y. M. Ruigrok, and et al. Heritability of circle of willis variations in families with intracranial aneurysms. *Plos One*, 13(1), 2018.

[13] Z. Vrselja, H. Brkic, S. Mrdenovic, R. Radic, and G. Curic. Function of circle of willis. *Journal of Cerebral Blood Flow Metabolism*, 34(4):578â584, 2014.

[14] D. E. Haines and G. A. Mihailoff. *Fundamental neuroscience for basic and clinical applications*. Elsevier, 2018.

[15] M. Toussaint. Numerical analysis of hemodynamics in intracranial aneurysms - proposing a third hemodynamic criterion for predicting rupture sites. *Master Thesis*, 2018.

[16] B. Eftekhar, M. Dadmehr, S. Ansari, M. Ghodsi, B. Nazparvar, and E. Ketabchi. Are the distributions of variations of circle of willis different in different populations? â results of an anatomical study and review of literature. *BMC Neurology*, 6(1), 2006.

[17] M. K. Pugsley and R. Tabrizchi. The vascular system: An overview of structure and function. *Journal of Pharmacological and Toxicological Methods*, 44(2):333â340, 2000.

[18] N. K. Rooij, B. K. Velthuis, A. Algra, and G. J. E. Rinkel. Configuration of the circle of willis, direction of flow, and shape of the aneurysm as risk factors for rupture of intracranial aneurysms. *Journal of Neurology*, 256(1):45â50, 2009.

[19] D. Katritsis, L. Kaiktsis, A. Chaniotis, J. Pantos, E. P. Efstathopoulos, and V. Marmarelis. Wall shear stress: Theoretical considerations and methods of measurement. *Progress in Cardiovascular Diseases*, 49(5):307â329, 2007.

[20] S. E. Razavi and R. Sahebjam. Numerical simulation of the blood flow behavior in the circle of willis. *BioImpacts*, 4(2):89–94, jun 2014.

[21] H.E.A van der Akker and R.F Mudde. *Transport phenomena: the art of balancing*. Delft Academic Press, 2014.

[22] P. H. Geoghegan, N. A. Buchmann, J. Soria, and M. C. Jermy. Time-resolved piv measurements of the flow field in a stenosed, compliant arterial model. *Experiments in Fluids*, 54(5), 2013.

[23] B. B. Lieber, A. P. Stancampiano, and A. K. Wakhloo. Alteration of hemodynamics in aneurysm models by stenting: Influence of stent porosity. *Annals of Biomedical Engineering*, 25(3):460â469, 1997.

[24] S. Gurzing. Particle image velocimetry on a patient-specific intracranial aneurysm. *Master Thesis*, 2019.

[25] N. Westerhof, M. I. M. Noble, N. Stergiopulos, and B. E. Westerhof. *Snapshots of hemodynamics: an aid for clinical research and graduate education*. Springer, 2019.

[26] A. Sandoo, J.C.S. Veldhuijzen Van Zanten, J, G. S. Metsios, D. Carroll, and G. D. Kitas. The endothelium and its role in regulating vascular tone. *The Open Cardiovascular Medicine Journal*, 4(1):302â312, 2010.

[27] Z. Kulcsar, A. Ugron, M. Marosfoi, Z. Berentei, G. Paal, and I. Szikora. Hemodynamics of cerebral aneurysm initiation: The role of wall shear stress and spatial wall shear stress gradient. *American Journal of Neuroradiology*, 32(3):587â594, Oct 2011.

[28] H. Meng, Z. Wang, Y. Hoi, L. Gao, E. Metaxa, D. D. Swartz, and J. Kolega. Complex hemodynamics at the apex of an arterial bifurcation induces vascular remodeling resembling cerebral aneurysm initiation. *Stroke*, 38(6):1924â1931, 2007.

[29] C. Sadasivan, D. J. Fiorella, H. H. Woo, and B. B. Lieber. Physical factors effecting cerebral aneurysm pathophysiology. *Annals of Biomedical Engineering*, 41(7):1347â1365, Mar 2013.

[30] L.-D. Jou, D.H. Lee, H. Morsi, and M.E. Mawad. Wall shear stress on ruptured and unruptured intracranial aneurysms at the internal carotid artery. *American Journal of Neuroradiology*, 29(9):1761â1767, Mar 2008.

[31] J. Xiang, S. K. Natarajan, M. Tremmel, D. Ma, J. Mocco, L. Nelson Hopkins, A. H. Siddiqui, E. I. Levy, and H. Meng. Hemodynamicâmorphologic discriminants for intracranial aneurysm rupture. *Stroke*, 42(1):144â152, 2011.

[32] T. Qiu, G. Jin, H. Xing, and H. Lu. Association between hemodynamics, morphology, and rupture risk of intracranial aneurysms: a computational fluid modeling study. *Neurological Sciences*, 38(6):1009â1018, Nov 2017.

[33] J. R. Cebral, M. Vazquez, D. M. Sforza, G. Houzeaux, S. Tateshima, E. Scrivano, C. Bleise, P. Lylyk, and C. M. Putman. Analysis of hemodynamics and wall mechanics at sites of cerebral aneurysm rupture. *Journal of NeuroInterventional Surgery*, 7(7):530â536, 2014.

[34] G. A. Einstein, S. Aishwarya, V. Sreeja, and S. Nandhini. Computational fluid dynamics for intracranial aneurysm rupture prediction and post-treatment hemodynamic analysis. *Lecture Notes in Bioengineering Computer Methods in Biomechanics and Biomedical Engineering*, page 1â10, 2017.

[35] R. Amaya, L. M. Cancel, and J. M. Tarbell. Interaction between the stress phase angle (spa) and the oscillatory shear index (osi) affects endothelial cell gene expression. *Plos One*, 11(11), 2016.

[36] J.R. Cebral, F. Mut, J. Weir, and C.M. Putman. Association of hemodynamic characteristics and cerebral aneurysm rupture. *American Journal of Neuroradiology*, 32(2):264â270, Apr 2010.

[37] Shu Chien. Mechanotransduction and endothelial cell homeostasis: the wisdom of the cell. *American Journal of Physiology-Heart and Circulatory Physiology*, 292(3):H1209–H1224, 2007. PMID: 17098825.

[38] V. Peiffer, S. J. Sherwin, and P. D. Weinberg. Computation in the rabbit aorta of a new metric â the transverse wall shear stress â to quantify the multidirectional character of disturbed blood flow. *Journal of Biomechanics*, 46(15):2651â2658, 2013.

[39] Yumnah Mohamied, Ethan M. Rowland, Emma L. Bailey, Spencer J. Sherwin, Martin A. Schwartz, and Peter D. Weinberg. Change of direction in the biomechanics of atherosclerosis. *Annals of Biomedical Engineering*, 43(1):16â25, 2014.

[40] A. J. Geers, H. G. Morales, I. Larrabide, C. Butakoff, P. Bijlenga, and A. F. Frangi. Wall shear stress at the initiation site of cerebral aneurysms. *Biomechanics and Modeling in Mechanobiology*, 16(1):97â115, 2016.

[41] Peter R. Mercer. Relative convexity and quadrature rules for the riemann-stieltjes integral. *Journal of Mathematical Inequalities*, (1):65â68, 2012.

[42] N. A. Buchmann, C. Atkinson, M. C. Jeremy, and J. Soria. Tomographic particle image velocimetry investigation of the flow in a modeled human carotid artery bifurcation. *Experiments in Fluids*, 50(4), Apr 2011.

[43] R. J. Adrian. Twenty years of particle image velocimetry. *Experiments in Fluids*, 39(2):159â169, Jun 2005.

[44] J Westerweel. Fundamentals of digital particle image velocimetry. *Measurement Science and Technology*, 8(12):1379â1392, Jan 1997.

[45] Nicolas A. Buchmann, Mark C. Jermy, and Chuong V. Nguyen. Experimental investigation of carotid artery haemodynamics in an anatomically realistic model. *International Journal of Experimental and Computational Biomechanics*, 1(2):172, 2009.

[46] J. Bale-Glickman, K. Selby, D. Saloner, and OÂ¨. SavasÂ¸. Experimental flow studies in exact-replica phantoms of atherosclerotic carotid bifurcations under steady input conditions. *Journal of Biomechanical Engineering*, 125(1):38â48, Jan 2003.

[47] Markus Raffel, Christian E. Willert, Steve T. Wereley, and JÃ$\frac{1}{4}$rgen Kompenhans. Particle image velocimetry. 2007.

[48] Matthew D. Ford, Hristo N. Nikolov, Jaques S. Milner, Stephen P. Lownie, Edwin M. Demont, Wojciech Kalata, Francis Loth, David W. Holdsworth, and David A. Steinman. Piv-measured versus cfd-predicted flow dynamics in anatomically realistic cerebral aneurysm models. *Journal of Biomechanical Engineering*, 130(2), Jan 2008.

[49] Xiaolin Wu. Patient specfic arterial flows via particle image velocimetry. 2019.

[50] D. Hasler, A. Landolt, and D. Obrist. Tomographic piv behind a prosthetic heart valve. *Experiments in Fluids*, 57(5), 2016.

[51] Gerrit Einte Elsinga. Tomographic particle image velocimetry and its application to turbulent boundary layers. 2008.

[52] Gerrit E Elsinga, Fulvio Scarano, Bernhard Wieneke, and Bas W van Oudheusden. Tomographic particle image velocimetry. *Experiments in fluids*, 41(6):933–947, 2006.

[53] Aswin Muralidharan. In-vitro validation of cardiovascular flows usign particle image velocimetry. a patient specific validation study. *Master Thesis*, 2017.

[54] Kendall D Dennis, Timothy L Rossman, David F Kallmes, and Dan Dragomir-Daescu. Intraaneurysmal flow rates are reduced by two flow diverters: an experiment using tomographic particle image velocimetry in an aneurysm model. *Journal of NeuroInterventional Surgery*, 7(12):937–942, 2015.

[55] Jonas Hamann. *Single Camera Stereoscopic Particle Image Velocimetry Conducted On Patient Specific Blood Flow Signal Controlled By Direct Valve Steering*, Nov 2019.

[56] A.f. Stalder, M.f. Russe, A. Frydrychowicz, J. Bock, J. Hennig, and M. Markl. Quantitative 2d and 3d phase contrast mri: Optimized analysis of blood flow and vessel wall parameters. *Magnetic Resonance in Medicine*, 60(5):1218â1231, 2008.

[57] A. Alimi. *Modeling and Numerical Simulation of Fluid-Structure Interaction in Circle of Willis*. Kassel University Press, 2020.

[58] J. Xiang, M. Tremmel, J. Kolega, E. I Levy, S. K Natarajan, and H. Meng. Newtonian viscosity model could overestimate wall shear stress in intracranial aneurysm domes and underestimate rupture risk. *Journal of NeuroInterventional Surgery*, 4(5):351â357, 2011.

[59] Yumnah Mohamied, Spencer J. Sherwin, and Peter D. Weinberg. Understanding the fluid mechanics behind transverse wall shear stress. *Journal of Biomechanics*, 50:102â109, 2017.

[60] A Mantha, Christof Karmonik, G Benndorf, C Strother, and Ralph Metcalfe. Hemodynamics in a cerebral artery before and after the formation of an aneurysm. *American Journal of Neuroradiology*, 27(5):1113–1118, 2006.

Appendices

1 Set-up equipment

Flowloop:

1. Bath temperature regulator: Julab Corio CD, Germany
2. The diaphragm: liquid pump NF 1.600 KPDC, KNF, Germany, 20 V and 2.05 A (DC Power Supply 6005 D, PeaktechÂ®, Germany)
3. flowmeter: Mini Cori-Flow MT5, Bronkhorst, the Netherlands
4. Control Valve: F-004AC/AI (NC), Bronkhorst, the Netherlands
5. Control software (flowmeter valve): FlowDDE by Bronkhorst

Optical set-up:

1. CMOS camera: 2016x2016 pixel, 12 bit, Imager pro HS 4M, LaVision Inc, England
2. Lens: 100 mm T3.1 macro lens, Samyang optics co LTD., Korea
3. Phantom slider: UnislideÂ® A6000, LG Motion, England
4. Laser: lDY304, Litron lasers, England $\lambda = 527nm$

2 Convert Macro

DaVis creates for each picture and for each time a separate data file which takes a long time to load into Tecplot. To decrease the loading time of Tecplot significantly a convert Macro was written in Tecplot and is shown here. This macro will make Tecplot convert a data file (.dat) in ASCII DAT data format to a data file (.plt) in Tecplot PLT binary format. With this done the loading time is much lower which increases the convenience a lot.

```
#!MC 1410

$!VarSet |numDigits| = ""
$!VarSet |FileBase| = ""
$!VarSet |StartNumber| = ""
$!VarSet |increment| = ""
$!VarSet |numberoffiles| = ""

$!PROMPTFORTEXTSTRING |numDigits|
    INSTRUCTIONS = "Number of digits in filename"
$!PROMPTFORTEXTSTRING |FileBase|
    INSTRUCTIONS = "Base filename"
$!PROMPTFORTEXTSTRING |StartNumber|
```

```
14      INSTRUCTIONS = "Start Number"
15 $!PROMPTFORTEXTSTRING |increment|
16      INSTRUCTIONS = "Increment of file numbers"
17 $!PROMPTFORTEXTSTRING |numberoffiles|
18      INSTRUCTIONS = "Number of total files"
19
20
21
22 $!LOOP |numberoffiles|
23 $!VARSET |add| = ((|LOOP|*|increment|)+|StartNumber|)
24 $!VARSET |n| = "|add|"
25
26 # format file numbers to correct digits
27
28 $!If |numDigits| == 0
29    $!VarSet |finalN| = "|n|"
30 $!ElseIf |numDigits| == 1
31    $!VarSet |finalN| = "|n|" # no use in formatting here
32 $!ElseIf |numDigits| == 2
33   $!VarSet |finalN| = "|n%02d|"
34 $!ElseIf |numDigits| == 3
35   $!VarSet |finalN| = "|n%03d|"
36 $!ElseIf |numDigits| == 4
37   $!VarSet |finalN| = "|n%04d|"
38 $!ElseIf |numDigits| == 5
39   $!VarSet |finalN| = "|n%05d|"
40 $!ElseIf |numDigits| == 6
41   $!VarSet |finalN| = "|n%06d|"
42 $!Endif
43
44 #$!PAUSE "|macrofilepath|\|FileBase||finalN|.plt"
45
46 #Checks to see if the file exists
47 $!EXTENDEDCOMMAND
48 COMMANDPROCESSORID = "extendmcr"
49 Command = 'QUERY.FILEEXISTS "|FileBase||finalN|.plt" "exists"'
50 $!IF "|exists|" == "YES"
51      $!READDATASET "|FileBase||finalN|.plt"
52        READDATAOPTION = APPEND
53 $!ENDIF
54
55 $!ENDLOOP
```

3 WSS Calculating Macro

The Tecplot macro that was used to alter the DaVis Data so it was ready to be imported into Python for further calculations.

```
#!MC 1410
#$!INCLUDEMACRO "load.mcr"
$!DRAWGRAPHICS FALSE
$!PROMPTFORTEXTSTRING |numDigits|
    INSTRUCTIONS = "Number of Iterations"
$!PROMPTFORTEXTSTRING |BeginTime|
    INSTRUCTIONS = "Begin Time first iteration (x.xxx sec)"
$!PROMPTFORTEXTSTRING |EndTime|
    INSTRUCTIONS = "End time last iteration (x.xxx sec)"
#Step_1
$!AlterData
  Equation = '{x [m]}={x [mm]}/1000'
$!AlterData
  Equation = '{y [m]}={y [mm]}/1000'
$!AlterData
  Equation = '{z [m]}={z [mm]}/1000'
#Step_2
$!ThreeDAxis XDetail{VarNum = 8}
$!ThreeDAxis YDetail{VarNum = 9}
$!ThreeDAxis ZDetail{VarNum = 10}
#Step_3
$!AlterData
  Equation = '{Vmagnitude}=sqrt({Vx [m/s]}**2+{Vy [m/s]}**2+{Vz [m/s]}**2)'
#Step_4
$!ExtendedCommand
  CommandProcessorID = 'CFDAnalyzer4'
  Command = 'SetFieldVariables ConvectionVarsAreMomentum=\'F\' UVar=4 VVar=5 WVar=6
      ID1=\'NotUsed\' Variable1=0 ID2=\'NotUsed\' Variable2=0'
#Step_5
$!ExtendedCommand
  CommandProcessorID = 'CFDAnalyzer4'
  Command = 'Calculate Function=\'VELOCITYGRADIENT\' Normalization=\'None\'
      ValueLocation=\'Nodal\' CalculateOnDemand=\'F\'
      UseMorePointsForFEGradientCalculations=\'F\''
#Creating correct workspace
$!IsoSurfaceLayers Show = Yes
$!IsoSurfaceAttributes 1  DefinitionContourGroup = 7
$!IsoSurfaceAttributes 1  Isovalue1 = 0.5

#Looping step 6,7
# Choose the constants of the Loop
$!VARSET |zone_select| = 1            #First zone
$!VARSET |NUMBEROFLOOPS| = |numDigits|      #Number of iterations
```

```
$!VARSET |begin_time| = |BeginTime|        #Begin time data set
$!VARSET |end_time| = |Endtime|          #End time data set

$!VARSET |Number_ofsteps| = (|NUMBEROFLOOPS|-1)
$!VARSET |zone_destination| = (|NUMBEROFLOOPS|+1)



$!LOOP |NUMBEROFLOOPS|
  $!GlobalTime SolutionTime = (|begin_time|+((((|end_time|-|begin_time|)/(|
      Number_ofsteps|))*(|LOOP|-1)))
  $!Smooth
    Zone = |zone_select|
    Var = 7
    NumSmoothPasses = 20
    SmoothWeight = 0.5
    SmoothBndryCond = Fixed
  $!ExtractIsoSurfaces
    Group = 1
    ExtractMode = SingleZone
  $!LinearInterpolate
    SourceZones =  [|zone_select|]
    DestinationZone = |zone_destination|
     VarList =  [12-20]
     LinearInterPConst = 0
     LinearInterpMode = DontChange
  $!VARSET |zone_select| +=1
  $!VARSET |zone_destination| +=1

$!ENDLOOP

#Step_8
$!ExtendedCommand
  CommandProcessorID = 'CFDAnalyzer4'
  Command = 'Calculate Function=\'GRIDKUNITNORMAL\' Normalization=\'None\'
      ValueLocation=\'Nodal\' CalculateOnDemand=\'F\'
      UseMorePointsForFEGradientCalculations=\'F\''
#Step_9
$!AlterData
  Equation = '{mu}= 0.0035'
$!AlterData
  Equation = '{T11} ={mu}* (2 * {dUdX})'
$!AlterData
  Equation = '{T12} = {mu} * ({dVdX} + {dUdY})'
$!AlterData
  Equation = '{T13} = {mu}* ({dWdX} + {dUdZ})'
$!AlterData
```

```
85    Equation = '{T22} = {mu} * (2 * {dVdY} )'
86  $!AlterData
87    Equation = '{T23} = {mu} * ({dVdZ} + {dWdY})'
88  $!AlterData
89    Equation = '{T33} = {mu} * (2 * {dWdZ})'
90  $!AlterData
91    Equation = '{taux} = {T11} * {X Grid K Unit Normal} + {T12} * {Y Grid K Unit
          Normal} + {T13} * {Z Grid K Unit Normal}'
92  $!AlterData
93    Equation = '{tauy} = {T12} * {X Grid K Unit Normal} + {T22} * {Y Grid K Unit
          Normal} + {T23} * {Z Grid K Unit Normal}'
94  $!AlterData
95    Equation = '{tauz} = {T13} * {X Grid K Unit Normal} + {T23} * {Y Grid K Unit
          Normal} + {T33} * {Z Grid K Unit Normal}'
96  $!AlterData
97    Equation = '{Tau} = sqrt({taux}*{taux}+{tauy}*{tauy}+{tauz}*{tauz})'
```

4 WSS Calculation

Preceding Wall Shear Stress calculations which were used in the Tecplot macro.

$$mu = 0.0035 \tag{14}$$

$$\tau_{11} = \mu * (dUdX + dUdX) \tag{15}$$

$$\tau_{12} = \mu * (dVdX + dUdY) \tag{16}$$

$$\tau_{13} = \mu * (dWdX + dUdZ) \tag{17}$$

$$\tau_{22} = \mu * (dVdY + dVdY) \tag{18}$$

$$\tau_{23} = \mu * (dVdZ + dWdY) \tag{19}$$

$$\tau_{33} = \mu * (dWdZ + dWdZ) \tag{20}$$

$$\tau_x = \tau_{11} * (XGridKUnitNormal) + \tau_{12} * (YGridKUnitNormal) + \tau_{13} * (ZGridKUnitNormal) \tag{21}$$

$$\tau_y = \tau_{12} * (XGridKUnitNormal) + \tau_{22} * (YGridKUnitNormal) + \tau_{23} * (ZGridKUnitNormal) \tag{22}$$

$$\tau_z = \tau_{13} * (XGridKUnitNormal) + \tau_{23} * (YGridKUnitNormal) + \tau_{33} * (ZGridKUnitNormal) \tag{23}$$

5 Python script

The Python script which was used to calculate the hemodynamic quantities for this research.

```
import tecplot as tp
import numpy as np
import tpmath_edit as tpmath
import tputils

tp.session.connect()

in_strand = 2
print("The time strand =", in_strand)
dataset = tp.active_frame().dataset

zones_by_strand = tputils.get_zones_by_strand(dataset)
strand_to_average = int(in_strand)
source_zones = zones_by_strand[strand_to_average]

N=35000
length = len(source_zones)
Array_length = 32140
#length = 3

#calculating total Time
first_time = source_zones[0].solution_time
Last_time = source_zones[length-1].solution_time
T =  Last_time - first_time
print("T =", T, "Sec")

print("Calculating: ")

##The code for retrieving a variable from multiple zones and summing them up and
    calculating the average.
# done for taux

print("  -  ",  dataset.variable(30).name)
taux = np.zeros((length,N))
i = 0
for i in range(length):
  # zone = source_zones[i]
  # taux = zone.values("taux")
  # taux_array = np.array(taux[:])
  # taux_new = np.pad(taux_array , (0, N-taux_array .size), 'constant')
  #one line
  taux_new = np.pad(np.array(source_zones[i].values(30)[:]) , (0, N-np.array(
      source_zones[i].values(30)[:]).size), 'constant')

```

```
43    taux[i] = taux_new
44    i += 1
45
46  #calculating sum of taux for every cell
47  taux_sum = np.sum(taux, axis = 0)
48
49  ##The code for retrieving a variable from multiple zones and summing them up and
        calculating the average.
50  # done for tauy
51
52  print(" - ", dataset.variable(31).name)
53  tauy = np.zeros((length,N))
54  i = 0
55  for i in range(length):
56    tauy_new = np.pad(np.array(source_zones[i].values(31)[:]) , (0, N-np.array(
          source_zones[i].values(31)[:]).size), 'constant')
57    tauy[i] = tauy_new
58    i += 1
59
60  #calculating sum of tauy for every cell
61  tauy_sum = np.sum(tauy, axis = 0)
62
63  ##The code for retrieving a variable from multiple zones and summing them up and
        calculating the average.
64  # done for tauz
65
66  print(" - ", dataset.variable(32).name)
67  tauz = np.zeros((length,N))
68  i = 0
69  for i in range(length):
70    tauz_new = np.pad(np.array(source_zones[i].values(32)[:]) , (0, N-np.array(
          source_zones[i].values(32)[:]).size), 'constant')
71    tauz[i] = tauz_new
72    i += 1
73
74  #calculating sum of tauz for every cell
75  tauz_sum = np.sum(tauz, axis = 0)
76
77  ##The code for retrieving a variable from multiple zones and summing them up and
        calculating the average.
78  # done for tau
79  print(" - ", dataset.variable(33).name)
80  tau = np.zeros((length,N))
81  i = 0
82  for i in range(length):
83    # zone1 = source_zones[i]
84    # taux1 = zone1.values("taux")
```

```
85    # taux1_array = np.array(taux1[:])
86    # taux1_new = np.pad(taux1_array , (0, N-taux1_array .size), 'constant')
87    # #one line
88    tau_new = np.pad(np.array(source_zones[i].values('Tau')[:]) , (0, N-np.array(
          source_zones[i].values('Tau')[:]).size), 'constant')
89    tau[i] = tau_new
90
91    i += 1
92
93 #calculating sum of tau for every cell
94 tau_sum = np.sum(tau, axis = 0)
95
96 # calculating Kx vector for the surface
97 print(" - ", dataset.variable(20).name)
98 Kx = np.zeros((length,N))
99 i = 0
100 for i in range(length):
101   # zone1 = source_zones[i]
102   # taux1 = zone1.values("taux")
103   # taux1_array = np.array(taux1[:])
104   # taux1_new = np.pad(taux1_array , (0, N-taux1_array .size), 'constant')
105   # #one line
106   Kx_new = np.pad(np.array(source_zones[i].values(20)[:]) , (0, N-np.array(
          source_zones[i].values(20)[:]).size), 'constant')
107   Kx[i] = Kx_new
108   i += 1
109
110 #calculating sum of Kx for every cell
111 Kx_sum = np.sum(Kx, axis = 0)
112
113 # calculating Ky vector for the surface
114 print(" - ", dataset.variable(21).name)
115 Ky = np.zeros((length,N))
116 i = 0
117 for i in range(length):
118   # zone1 = source_zones[i]
119   # taux1 = zone1.values("taux")
120   # taux1_array = np.array(taux1[:])
121   # taux1_new = np.pad(taux1_array , (0, N-taux1_array .size), 'constant')
122   # #one line
123   Ky_new = np.pad(np.array(source_zones[i].values(21)[:]) , (0, N-np.array(
          source_zones[i].values(21)[:]).size), 'constant')
124   Ky[i] = Ky_new
125   i += 1
126
127 #calculating sum of Ky for every cell
128 Ky_sum = np.sum(Ky, axis = 0)
```

```
129
130 # calculating Kz vector for the surface
131 print(" - ", dataset.variable(22).name)
132 Kz = np.zeros((length,N))
133 i = 0
134 for i in range(length):
135   # zone1 = source_zones[i]
136   # taux1 = zone1.values("taux")
137   # taux1_array = np.array(taux1[:])
138   # taux1_new = np.pad(taux1_array , (0, N-taux1_array .size), 'constant')
139   # #one line
140   Kz_new = np.pad(np.array(source_zones[i].values(22)[:]) , (0, N-np.array(
          source_zones[i].values(22)[:]).size), 'constant')
141   Kz[i] = Kz_new
142   i += 1
143
144 #calculating sum of Kz for every cell
145 Kz_sum = np.sum(Kz, axis = 0)
146
147 # calculating TAWSS
148 TAWSS = tau_sum/length
149
150 #Calculating OSI
151 tau_up = (np.sqrt(np.power(taux_sum,2)+ np.power(tauy_sum,2) +np.power(tauz_sum,2))
      )/length
152 OSI = 0.5*(1-(tau_up/TAWSS))
153
154 #Calculating Trans WSS
155 f = (np.sqrt(np.power(taux_sum,2)+ np.power(tauy_sum,2) +np.power(tauz_sum,2)))/
      length
156 x_hat = ( Ky*tauz_sum/length - Kz*tauy_sum/length)/f
157 y_hat = ( Kz*taux_sum/length - Kx*tauz_sum/length)/f
158 z_hat = ( Kx*tauy_sum/length - Ky*taux_sum/length)/f
159 TRANSWSS_x = np.multiply(taux ,x_hat)
160 TRANSWSS_y = np.multiply(tauy ,y_hat)
161 TRANSWSS_z = np.multiply(tauz ,z_hat)
162 TRANSWSS_magnitude = (np.sqrt(np.power(TRANSWSS_x,2)+ np.power(TRANSWSS_y,2) +np.
      power(TRANSWSS_z,2)))
163 TRANSWSS = np.sum(TRANSWSS_magnitude, axis = 0)/length
164
165 # calculating CFI
166 CFI_up = TRANSWSS_x + TRANSWSS_y + TRANSWSS_z
167 CFI_down = tau_sum
168 CFI = np.sum((CFI_up/CFI_down), axis = 0)/leng
169
170 # Printing the values
171 print("taux_sum =", taux_sum)
```

```
172 print("tauy_sum =", tauy_sum)
173 print("tauz_sum =", tauz_sum)
174 print("OSI =", OSI)
175 print("TAWSS =", TAWSS)
176 print("TRANSWSS =", TRANSWSS)
177 print("CFI =", CFI)
178
179 taux_sum_T = np.transpose(taux_sum)
180 tauy_sum_T = np.transpose(tauy_sum)
181 tauz_sum_T = np.transpose(tauz_sum)
182 OSI_T = np.transpose(OSI)
183 TAWSS_T = np.transpose(TAWSS)
184 TRANSWSS_T = np.transpose(TRANSWSS)
185 CFI_T = np.transpose(CFI)
186
187 dataset.add_variable('taux_sum')
188 dataset.add_variable('tauy_sum')
189 dataset.add_variable('tauz_sum')
190 dataset.add_variable('TAWSS')
191 dataset.add_variable('OSI')
192 dataset.add_variable('TRANSWSS')
193 dataset.add_variable('CFI')
194
195 print(source_zones[length-1])
196 zone = source_zones[length-1]
197
198 # Fill the dataset
199 taux_sum = taux_sum[0:Array_length]
200 tauy_sum = tauy_sum[0:Array_length]
201 tauz_sum = tauz_sum[0:Array_length]
202 TAWSS = TAWSS[0:Array_length]
203 OSI = OSI[0:Array_length]
204 TRANSWSS = TRANSWSS[0:Array_length]
205 CFI = CFI[0:Array_length]
206
207 zone.values('taux_sum')[:] = taux_sum
208 zone.values('tauy_sum')[:] = tauy_sum
209 zone.values('tauz_sum')[:] = tauz_sum
210 zone.values('TAWSS')[:] = TAWSS
211 zone.values('OSI')[:] = OSI
212 zone.values('TRANSWSS')[:] = TRANSWSS
213 zone.values('CFI')[:] = CFI
```

6 Data structure

In this subsection the used data-structure will be stated as will the wanted data structure be explained. The data structure that was implemented in this research depended on a Cartesian coordinate system where the x,y,z matrices were only filled where they had a non zero velocity. This means that everywhere outside the aneurysm no data entry was made. Due to the fact that the aneurysm boundary is not precisely approximated through Davis this results in a slight shift in how these matrices are appended. See the following figure for an example.

N \ V	x [mm]	y [mm]	z [mm]
1	-11.4213	-4.53212	-30.1357
2	-10.9155	-4.53212	-30.2261
3	-10.4097	-4.53212	-30.2596
4	-9.9039	-4.53212	-30.2693
5	-9.39808	-4.53212	-30.2698
6	-8.89227	-4.53212	-30.2628
7	-8.38645	-4.53212	-30.239
8	-7.88063	-4.53212	-30.1777
9	-11.4213	-5.03793	-30.2261
10	-10.9155	-5.03793	-30.3079
11	-10.4097	-5.03793	-30.3374
12	-9.9039	-5.03793	-30.3457
13	-9.39808	-5.03793	-30.3467
14	-8.89227	-5.03793	-30.3426
15	-8.38645	-5.03793	-30.3272
16	-7.88063	-5.03793	-30.2838
17	-7.37481	-5.03793	-30.1811
18	-11.4213	-5.54375	-30.2487
19	-10.9155	-5.54375	-30.3311
20	-10.4097	-5.54375	-30.3614
21	-9.9039	-5.54375	-30.3702
22	-9.39808	-5.54375	-30.3717
23	-8.89227	-5.54375	-30.3695
24	-8.38645	-5.54375	-30.3591
25	-7.88063	-5.54375	-30.3258
26	-7.37481	-5.54375	-30.2393
27	-11.4213	-6.04957	-30.2369
28	-10.9155	-6.04957	-30.3281
29	-10.4097	-6.04957	-30.3642

(a) x,y,z coordinates shown for time point 1

N \ V	x [mm]	y [mm]	z [mm]
1	-11.4213	-4.53212	-30.1298
2	-10.9155	-4.53212	-30.2075
3	-10.4097	-4.53212	-30.2188
4	-9.9039	-4.53212	-30.2002
5	-9.39808	-4.53212	-30.1756
6	-8.89227	-4.53212	-30.1485
7	-11.4213	-5.03793	-30.2265
8	-10.9155	-5.03793	-30.2999
9	-10.4097	-5.03793	-30.3171
10	-9.9039	-5.03793	-30.3105
11	-9.39808	-5.03793	-30.2974
12	-8.89227	-5.03793	-30.2772
13	-8.38645	-5.03793	-30.2335
14	-7.88063	-5.03793	-30.1418
15	-11.4213	-5.54375	-30.2546
16	-10.9155	-5.54375	-30.3277
17	-10.4097	-5.54375	-30.3497
18	-9.9039	-5.54375	-30.3508
19	-9.39808	-5.54375	-30.3439
20	-8.89227	-5.54375	-30.3262
21	-8.38645	-5.54375	-30.2807
22	-7.88063	-5.54375	-30.185
23	-11.4213	-6.04957	-30.2401
24	-10.9155	-6.04957	-30.3154
25	-10.4097	-6.04957	-30.3412
26	-9.9039	-6.04957	-30.3463
27	-9.39808	-6.04957	-30.3421
28	-8.89227	-6.04957	-30.3246
29	-8.38645	-6.04957	-30.2771

(b) x,y,z coordinates shown for time point 2

As can be seen is that Tecplot sorts the data in the following sequence: first y then x and z follows. When comparing these images and especially when comparing the rows it can be seen that

minor differences occur. These minor differences give when added with all the other time steps a contribution to the error and additionally incorrect images. In the discussion two solutions were given. One of these solutions would completely remove the error. This solution is to create a rigid coordinate structure in an earlier step in the research. If a rigid cube was created in x,y,z with coordinates with up till 5 decimals and the aneurysm data could be appended to this structure where the misaligned data would be interpolated to the nearest structure cell. This would give the same type of data sets only would the structure over every time point be constant and could they be added correctly together which would result in smooth images. This method may cost a lot more storage space and would be more time consuming. However, it would give a clearer image and much better results.

Cross-Flow index

In this section a new quantity is introduced. It is added in the Appendix due to the fact that its validity could not be confirmed and thus it needs more research to be mentioned as a result in the thesis.

A very new and not commonly known hemo-dynamic quantity is the Cross-Flow Index (CFI). This novel parameter is an addition on the Trans-WSS. CFI represents the directionality of the WSS where the magnitude of the WSS is not taken into account. In contrary to the Trans-WSS where the value depended on the TAWSS at that location. The CFI can also be seen as the sine of the angle between the temporal mean WSS and the instantaneous WSS [59]. The CFI is an index for the time-average of these instantaneous components defined below.

$$CFI = \frac{1}{T}\int_0^T \frac{\vec{\tau}_\omega}{|\vec{\tau}_\omega|} \cdot (\vec{n} \times \frac{\int_0^T \vec{\tau}_\omega dt}{\left|\int_0^T \vec{\tau}_\omega dt\right|})|dt \tag{24}$$

This fairly new hemo dynamic quantity was derived from another new but older hemo dynamic quantity. This quantity was called the (Potential) Aneurysm Formation Indicator (AFI). The AFI is the cosine between the temporal mean WSS and the instantaneous WSS [60].

Results of the Cross-Flow index

As described in section 6, the Cross-Flow Index (CFI) can be calculated using equation 24. The CFI is an index that can be seen as the change in direction of the WSS where the magnitude of the WSS is not taken into account. In figure 20 is the CFI visualized onto the aneurysm wall for 11, 21, 51 and 101 timepoints during a cardiac cycle

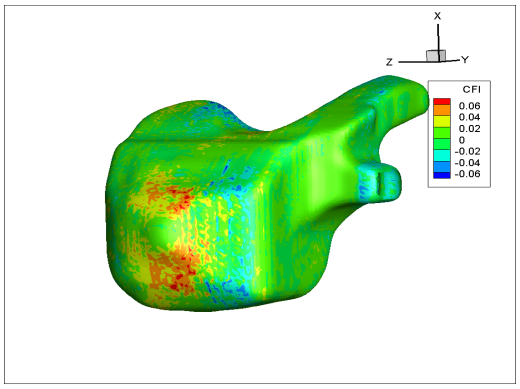

(a) The CFI is shown as contour on the aneurysm calculated for 11 timepoints.

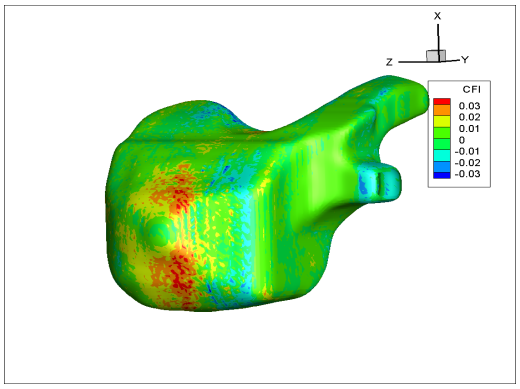

(b) The CFI is shown as contour on the aneurysm calculated for 21 timepoints.

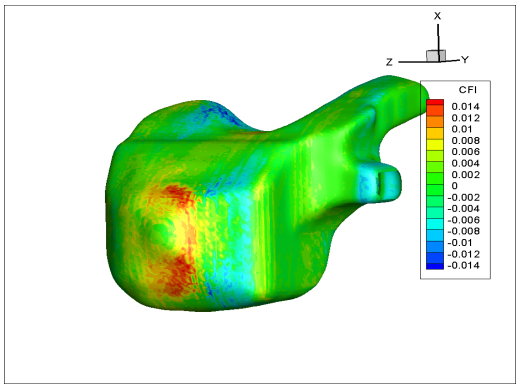

(c) The CFI is shown as contour on the aneurysm calculated for 51 timepoints.

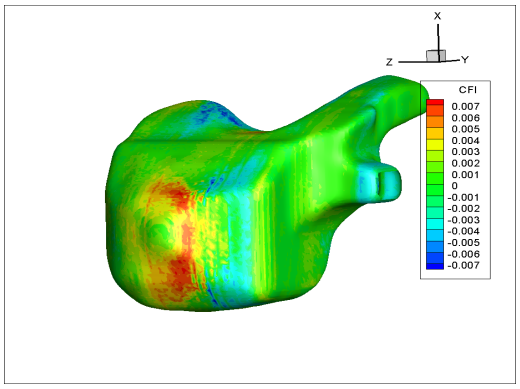

(d) The CFI is shown as contour on the aneurysm calculated for 101 timepoints.

Figure 20: In this image the CFI, calculated over the whole cardiac cycle, is projected onto the surface of the aneurysm for different amount of time steps in between.

When comparing these images with each other it can be seen that the images remain more or less the same. This is what is expected because this is the average over the whole cardiac cycle. In addition, it can be seen that the values become the same ratio smaller when adding this ratio of timepoints. This is due to the fact that the same outcome gets averaged over more timepoints. However, this is in indicator and it supports other hemo-dynamic quantities rather then being a stand alone quantity. In conclusion, to get a smooth result not more then 51 datapoints are needed.

The CFI can be seen as an index that displays the change in direction of the WSS where the magnitude of the WSS is not taken into account. In other words it can be seen as an indicator for the Trans-WSS when the value of the TAWSS is not taken into account. The Trans-WSS has low values in the bulge because the TAWSS was low there which can be seen in figure 17. However

the OSI showed high values which give reason to believe high directional change was measured there which can be seen in figure 16. The CFI shows that the flow here is not only uniaxial but multidirectional what should be expected in the aneurysm due to its turbulent nature during a cardiac cycle. However, this was not correctly shown in the Trans-WSS because it was surpassed by the other locations with high TAWSS.

Furthermore, when looking at the results of the CFI some peculiar things can be noticed. When looking at the inlet and outlet it can be seen that a zero value is reported. However this could not be the case due to the fact that the Trans-WSS reports a value.

In conclusion, the CFI has a lot to offer when researching the Trans-WSS and its contribution to the rupture risk of an aneurysm. However, it still needs more research to be reported as an actual results because the validity of these results can not be confirmed. It could be that an error was made in the coding of this quantity or that the understanding of this quantity is not good enough. Therefor, I have chosen to add this in the appendix to still show the potential of this quantity.